AGING

A genome-wide CRISPR-based screen identifies *KAT7* as a driver of cellular senescence

Wei Wang[1,2,3,4]*, Yuxuan Zheng[5,6]*, Shuhui Sun[1,3,4]*, Wei Li[7]*, Moshi Song[1,4,8], Qianzhao Ji[1,4], Zeming Wu[2,4], Zunpeng Liu[2,4], Yanling Fan[9,10], Feifei Liu[1], Jingyi Li[1,4], Concepcion Rodriguez Esteban[11], Si Wang[1,7,8], Qi Zhou[2,4,8], Juan Carlos Izpisua Belmonte[11], Weiqi Zhang[4,7,8,9,10†], Jing Qu[2,4,8†], Fuchou Tang[5,6†], Guang-Hui Liu[1,3,4,7,8†]

Understanding the genetic and epigenetic bases of cellular senescence is instrumental in developing interventions to slow aging. We performed genome-wide CRISPR-Cas9–based screens using two types of human mesenchymal precursor cells (hMPCs) exhibiting accelerated senescence. The hMPCs were derived from human embryonic stem cells carrying the pathogenic mutations that cause the accelerated aging diseases Werner syndrome and Hutchinson-Gilford progeria syndrome. Genes whose deficiency alleviated cellular senescence were identified, including *KAT7*, a histone acetyltransferase, which ranked as a top hit in both progeroid hMPC models. Inactivation of KAT7 decreased histone H3 lysine 14 acetylation, repressed $p15^{INK4b}$ transcription, and alleviated hMPC senescence. Moreover, lentiviral vectors encoding Cas9/sg-*Kat7*, given intravenously, alleviated hepatocyte senescence and liver aging and extended life span in physiologically aged mice as well as progeroid $Zmpste24^{-/-}$ mice that exhibit a premature aging phenotype. CRISPR-Cas9–based genetic screening is a robust method for systematically uncovering senescence genes such as *KAT7*, which may represent a therapeutic target for developing aging interventions.

INTRODUCTION

Aging is a seemingly inevitable process that causes functional decline in nearly all organisms. Cellular senescence, a state of permanent growth arrest, has recently emerged as both a hallmark of aging and a fundamental driver of the aging processes (*1*–*9*). Senescent cells accumulate in tissues over time, triggering natural features of organismal aging and contributing to aging-related diseases (for example, hepatic steatosis and osteoarthritis) (*1*, *3*, *4*, *6*, *8*–*10*). Prophylactic ablation of senescent cells expressing the senescence marker $p16^{INK4A}$ mitigates tissue degeneration and extends the health span in mice, indicating that senescent cells play a causative role in organismal aging (*6*, *11*). For example, senescent cells gradually accumulate in the degenerated liver, whereas clearing senescent cells from the liver attenuates the development of hepatic steatosis (*3*, *4*). Therefore, delaying or reversing cellular senescence may provide a new therapeutic approach for treating aging-related pathologies.

Understanding the genetic and epigenetic mechanisms of aging may inform the development of strategies that can delay cellular senescence (*12*, *13*).Candidate genetic pathways that regulate aging have been identified in genetic screens (*14*). However, only a few aging-associated genes have been identified directly on the basis of evidence from human or human cellular models (*12*–*15*). Therefore, elucidating the genetic programs that govern human aging remains an important goal. Forward genetic screens (also known as mutagenesis screen) are ideal tools for determining which human genes are involved in specific biological processes. Recently, the RNA-guided clustered regularly interspaced short palindromic repeat (CRISPR)–CRISPR-associated protein 9 (Cas9) gene-editing system has been used in combination with genome-scale single guide RNA (sgRNA) libraries for genome-wide screens of gene function (*16*, *17*). Such efforts have established CRISPR-Cas9–based gene inactivation as a powerful tool for genetic screening, complementary to RNA interference (RNAi) (*16*). To date, however, this approach has seldom been used to find genes involved in aging-related processes.

RESULTS

A genome-wide CRISPR-Cas9–based screen identifies new human senescence-promoting genes

Here, we performed a genome-wide CRISPR-Cas9–based loss-of-function screen in a stem cell model of Werner syndrome (WS) (fig. S1, A to D) (*18*, *19*), an ideal platform for identifying new senescence-promoting genes. To this end, we performed a lentiviral vector-based screen in WS human mesenchymal precursor cells (hMPCs) using a human CRISPR knockout pooled library [genome-scale CRISPR knockout v2 (GeCKOv2)] containing 123,411 unique sgRNAs targeting 19,050 annotated protein-coding genes and 1000 nontargeting control sgRNAs (sg-NTCs) (Fig. 1A) (*20*). To identify genes whose disruption restored cell proliferation and prevented cellular senescence,

[1]State Key Laboratory of Membrane Biology, Institute of Zoology, Chinese Academy of Sciences, Beijing, 100101, China. [2]State Key Laboratory of Stem Cell and Reproductive Biology, Institute of Zoology, Chinese Academy of Sciences, Beijing 100101, China. [3]National Laboratory of Biomacromolecules, CAS Center for Excellence in Biomacromolecules, Institute of Biophysics, Chinese Academy of Sciences, Beijing 100101, China. [4]University of Chinese Academy of Sciences, Beijing 100049, China. [5]Beijing Advanced Innovation Center for Genomics, Biomedical Pioneering Innovation Center, School of Life Sciences, Peking University, Beijing 100871, China. [6]Peking-Tsinghua Center for Life Sciences, Academy for Advanced Interdisciplinary Studies, Peking University, Beijing 100871, China. [7]Advanced Innovation Center for Human Brain Protection, National Clinical Research Center for Geriatric Disorders, Xuanwu Hospital Capital Medical University, Beijing 100053, China. [8]Institute for Stem Cell and Regeneration, Chinese Academy of Sciences, Beijing 100101, China. [9]CAS Key Laboratory of Genomic and Precision Medicine, Beijing Institute of Genomics, Chinese Academy of Sciences, Beijing 100101, China. [10]China National Center for Bioinformation, Chinese Academy of Sciences, Beijing 100101, China. [11]Gene Expression Laboratory, Salk Institute for Biological Studies, La Jolla, CA 92037, USA.
*These authors contributed equally to this work.
†Corresponding author. Email: ghliu@ioz.ac.cn (G.-H.L.); tangfuchou@pku.edu.cn (F.T.); qujing@ioz.ac.cn (J.Q.); zhangwq@big.ac.cn (W.Z.)

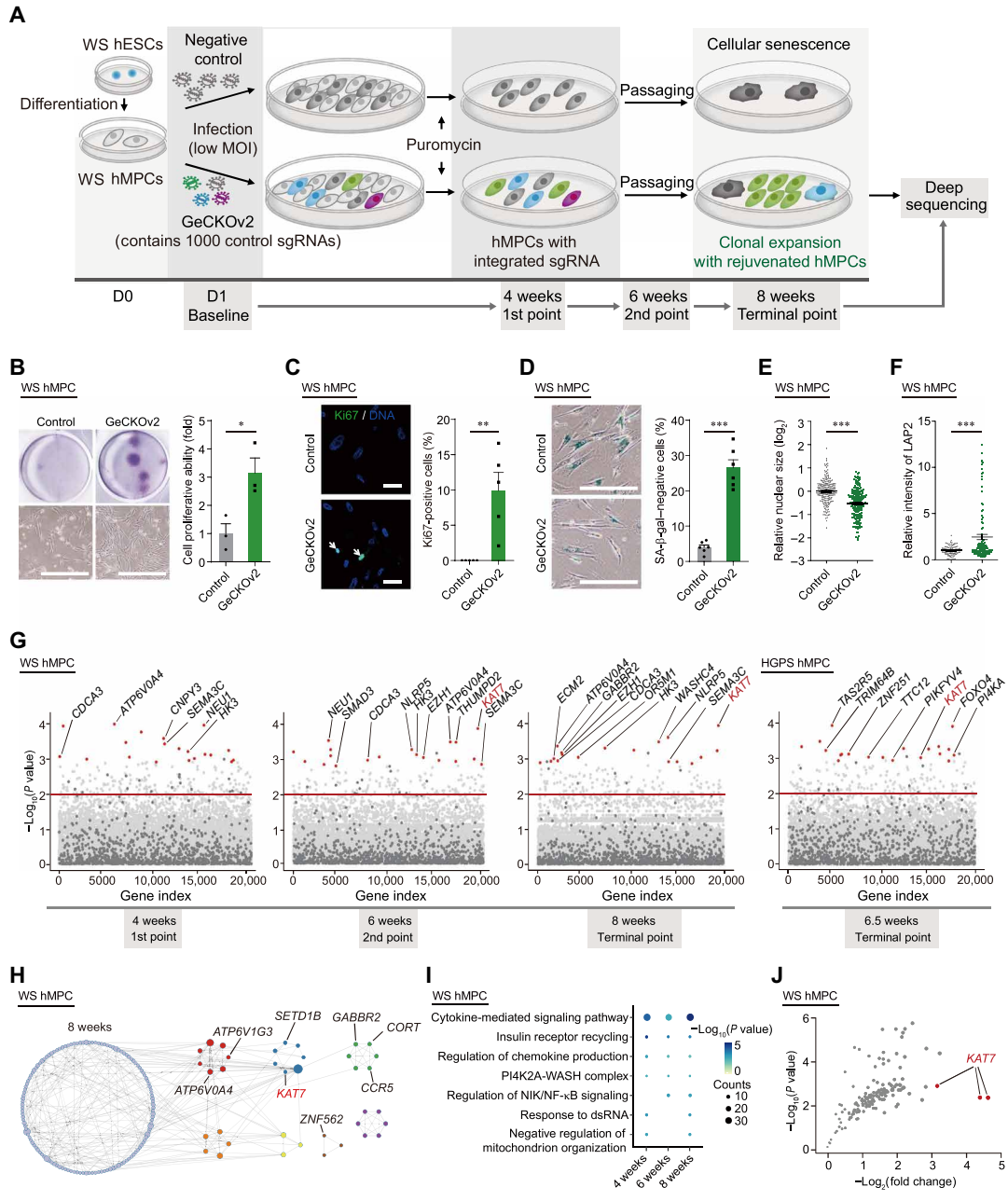

Fig. 1. A genome-wide CRISPR-Cas9–based screen for human senescence-promoting genes. (**A**) Schematic outlining the design of a CRISPR-Cas9–based screen to identify senescence-promoting genes in the WS premature aging hMPC model. Top row: Negative control (control) receiving six nontargeting control sgRNAs and becoming senescent at 8 weeks after virus infection. Bottom row: Experimental plates receiving genome-scale CRISPR knockout v2 (GeCKOv2) containing 123,411 unique sgRNAs targeting 19,050 annotated protein-coding genes plus 1000 nontargeting control sgRNAs and deeply sequenced at 4, 6, and 8 weeks to identify the clonal identity of rejuvenated hMPCs. (**B**) Top: Single-cell colony formation assay of WS hMPCs at 6 weeks after virus infection. Statistical results on the right. $n = 3$ biological replicates. Bottom: Light microscopic images of cells. Scale bars, 250 μm. Data are representative of three independent experiments. (**C**) Immunofluorescence analysis of Ki67 in WS hMPCs at 6.5 weeks after virus infection. The white arrows identify Ki67-positive cells. Scale bars, 50 μm. $n = 5$ biological replicates. (**D**) SA-β-gal staining of WS hMPCs at 6 weeks after virus infection. Scale bars, 100 μm. $n = 6$ biological replicates. (**E**) Quantification of the nuclear size of WS hMPCs at 6.5 weeks after virus infection; number of cells ≥ 280, cells from three biological replicates. (**F**) Immunofluorescence analysis of LAP2 expression in WS hMPCs at 6.5 weeks after virus infection; number of cells ≥ 100, cells from three biological replicates. (**G**) Enrichment score calculated for each gene based on its prevalence in the pool of WS hMPCs harvested at 4, 6, and 8 weeks (left and middle) and HGPS hMPCs harvested at 6.5 weeks (right) after viral infection relative to its prevalence in the GeCKOv2 library plasmid pool. Genes detected in the GeCKOv2 library are shown as dots in the diagram; the red dots indicate some of the top 20 enriched genes in the screen; the dark gray dots indicate nontargeting control sgRNAs. (**H**) Metascape visualization of genetic interaction network of the top 500 enriched genes in the screen of WS hMPCs at 8 weeks; the colored points indicate densely connected network components identified by the Molecular Complex Detection (MCODE) algorithm; some of the top 50 ranked genes in the screen of WS hMPCs at 8 weeks are as labeled. (**I**) Representative GO terms and pathways enriched in the top 500 enriched genes in the screen of WS hMPCs at 4, 6, and 8 weeks based on functional enrichment analysis ($P < 0.05$). Dot colors show statistical significance, and dot size indicates the number of genes in the corresponding GO terms. NF-κB, nuclear factor κB; NIK, NF-κB–inducing kinase; dsRNA, double-stranded RNA. (**J**) Scatter plot showing the result of SA-β-gal staining in which the top 50 ranked genes in the screen of WS hMPCs at 8 weeks were individually knocked out by three sgRNAs. The red dots indicate three sgRNAs of *KAT7*. $n = 3$ biological replicates. Data are presented as the means ± SEM. Comparisons were performed with two-tailed Student's *t* test. $^*P < 0.05$, $^{**}P < 0.01$, and $^{***}P < 0.001$.

we subjected transduced WS hMPCs to in vitro serial passaging (Fig. 1A). From 4 weeks after lentivirus transduction, we observed the progressive appearance of rejuvenated cell clones that had escaped premature senescence in WS hMPCs transduced with the on-target sgRNA library (Fig. 1B). After serial passaging, these rejuvenated WS hMPC clones became dominant and exhibited youthful features, including an increased percentage of Ki67-positive cells (Fig. 1C), decreased percentage of senescence-associated β-galactosidase (SA-β-gal)–positive cells (Fig. 1D), and improved nuclear architecture (Fig. 1, E and F, and fig. S1, E to G). In contrast, WS hMPCs

transduced with a mixture of sg-NTCs underwent progressive growth arrest during the screening process (Fig. 1, A to F) (*21*). These results indicate that the CRISPR-Cas9–mediated disruption of certain genes alleviates or reverses cellular senescence in WS hMPCs.

To identify the genes whose inactivation potentially delayed cellular senescence, we sequenced sgRNAs from rejuvenated WS hMPCs to determine sgRNA representation. Cells were collected at 4 weeks (when small clones appeared), at 6 weeks, and at 8 weeks (when WS hMPCs transduced with the sg-NTCs exhibited growth arrest) after infection. We observed that the global patterns of sgRNA distributions were distinct at different time points (Fig. 1G), revealed by shifts in the corresponding density distribution curves (fig. S1H). As shown in the Venn diagram of enriched target genes, most gene knockouts have already been enriched by 4 weeks (fig. S1I). Only a small fraction of highly enriched sgRNAs (up to 1.4%) were detected at 8 weeks (fig. S1J). We found that sgRNAs with decreased abundance were linked to genes required for fundamental cellular processes such as cell proliferation, indicating selection against cells that were compromised in such functions (fig. S1K). In contrast, as visualized in genetic interaction networks, sgRNAs with increased abundance at different time points were linked to genes involved in cytokine-mediated signaling pathway (*IFNB1*, *CCR5*, and *CCR8*) and negative regulation of mitochondrion organization (*MAPT*, *FZD9*, and *MUL1*) (Fig. 1, H and I, fig. S1L). We were encouraged to see that sgRNAs targeting *P53*, a well-established senescence-promoting gene, and senescence-associated secretory phenotype (SASP)–related genes (*MMP14*, *TNFRSF11B*, *MMP13*, *IL7*, and *TNFRSF1A*) were enriched after extended cell culture, providing proof of concept for our approach (fig. S1, M and N). Excitingly, we also identified more than 100 candidate senescence-promoting genes with their corresponding sgRNAs enriched throughout the screening process, including *KAT7* and *WASHC4* (Fig. 1G, fig. S1I and data file S1). The top 50 abundant sgRNAs enriched at 8 weeks after infection were transduced into WS hMPCs individually, and the effectiveness of these sgRNAs in promoting cellular rejuvenation was validated by SA-β-gal staining (Fig. 1J and data file S1). In addition to screening in WS hMPCs, we performed a similar screen using hMPCs derived from Hutchinson-Gilford progeria syndrome (HGPS)–specific human embryonic stem cells (hESCs) (bearing the heterozygous $LMNA^{G608G/+}$ mutation), which is another human cell model of premature aging (fig. S1, A and O, and summarized in fig. S1P) (*22*–*24*). About one-fifth of the enriched genes identified in WS-based assay were also identified in the HGPS-based screen, which may reflect both shared and divergent pathogenesis of these two premature aging disorders (Fig. 1G and fig. S1Q) (*19*, *25*). *KAT7*, encoding a histone acetyltransferase (*26*), was again identified as one of the top targets in alleviating cellular senescence (Fig. 1G).

Depletion of *KAT7* rejuvenates WS hMPCs

As *KAT7* was identified as the most effective knockout target in promoting cellular rejuvenation in both screens, we next asked by what molecular mechanisms *KAT7* regulates human cellular senescence in WS hMPCs. Using two different *KAT7*-targeting sgRNAs (Fig. 2A and fig. S2, A and B), we validated that *KAT7* depletion restored the compromised ability of WS hMPCs to differentiate into osteoblasts and adipocytes (fig. S2C) (*19*). In addition, *KAT7* deficiency substantially increased the proliferative potential of WS hMPCs upon serial passaging, albeit their cell growth arrest still occurred at the same passage as it did for wild-type (WT) hMPCs (Fig. 2B and fig. S2D). *KAT7* deficiency alleviated multiple premature aging phenotypes previously identified in WS hMPCs (*18*, *19*), as evidenced by the following findings: (i) increased percentage of Ki67-positive cells and cells in the S phase of the cell cycle (Fig. 2C and fig. S2E); (ii) decreased percentage of SA-β-gal–positive cells (Fig. 2D and fig. S2, F and G); (iii) decreased expression of aging-associated genes $p16^{INK4A}$ and $p21^{CIP1}$ and repressed DNA damage response (Fig. 2E and fig. S2, B and H); (iv) reduced secretion of interleukin-6 (IL-6), IL-1β, IL-8, and monocyte chemoattractant protein 1 (MCP1), indicating declined SASP (Fig. 2F and fig. S2I); and (v) attenuated functional decay of WS hMPCs implanted into the tibialis anterior muscle of nude mice (Fig. 2G). In addition, *KAT7* depletion reduced the proportion of apoptotic cells in WS hMPCs, indicating that depletion of *KAT7* alleviated cellular senescence, rather than eliminating senescent cells (fig. S2J). To investigate the possibility that loss of KAT7 in hMPCs may result in tumorigenic transformation, we subcutaneously injected *KAT7*-deficient WS hMPCs into immunodeficient mice. We monitored the mice for 8 months and observed no tumor formation (fig. S2K), consistent with a previous report that knockout of *KAT7* inhibits proliferation, rather than exerting a carcinogenic effect in tumor cells (*27*, *28*).

We observed that loss of *KAT7* effectively restored nuclear morphology (Fig. 2, A and H, and fig. S2L) (*18*, *19*) and mitigated nuclear lamina disorganization in WS hMPCs (Fig. 2, E and I, and fig. S2, B and M, and summarized in fig. S2N). Consistent with these observations, high-throughput chromosome conformation capture (Hi-C) analysis revealed the gain of long-range and loss of short-range chromosomal interactions upon *KAT7* depletion, which was opposite to the Hi-C interaction matrices of senescent cells (Fig. 2J and fig. S2, O to Q) (*29*, *30*). We also found that 10.7% of compartment A (which mostly contains active genes with euchromatin marks) switched to compartment B (which was predominantly transcriptionally inactive with constitutive heterochromatin marks) upon *KAT7* depletion, indicating restoration of the chromatin configuration of WS hMPCs to a more compact state, similar to that of young hMPCs (Fig. 2K). In addition, genome-wide RNA sequencing (RNA-seq) revealed that KAT7 depletion rescued the expression of nearly one-third (561 of 1779) of differentially expressed genes (DEGs) in WS hMPCs compared to WT hMPCs (Fig. 2L and data file S1) (*18*). Genes involved in chromosome organization and DNA packaging were reactivated upon *KAT7* depletion in WS hMPCs, resembling young hMPCs (Fig. 2M). Together, these results indicate that *KAT7* deficiency rejuvenates WS hMPCs by alleviating senescence phenotypes, restoring chromatin architecture, and resetting transcriptional profiles to resemble those of WT hMPCs.

KAT7 mediates senescence in other cellular models of human aging

To investigate whether *KAT7* deficiency would have a similar impact on other models of senescence, we assessed HGPS hMPCs and replicative-senescent (RS) hMPCs (*19*, *31*) and found that KAT7 ablation in both models improved proliferative potential and alleviated aging phenotypes (fig. S3, A to I). The expression of progerin (a mutant form of Lamin A) (*23*) was also decreased in *KAT7*-deficient HGPS hMPCs relative to sg-NTCs–transduced HGPS hMPCs (fig. S3, J and K). Furthermore, the ablation of KAT7 alleviated oncogene-, ultraviolet-, and H_2O_2-induced cellular senescence (fig. S4, A to D) (*14*), indicating that *KAT7* depletion attenuates senescence in diverse biological contexts.

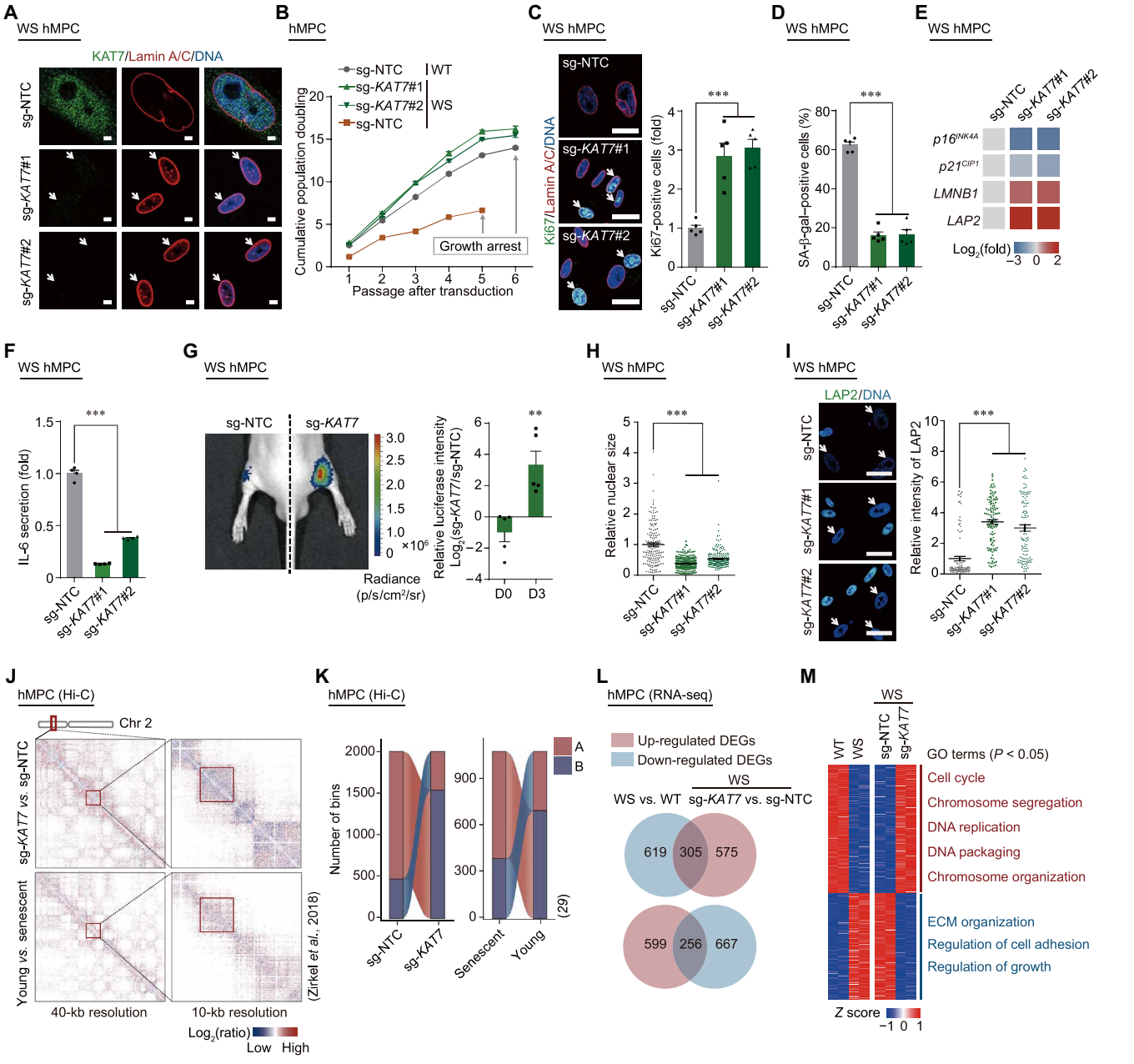

Fig. 2. Depletion of *KAT7* rejuvenates Werner syndrome hMPCs. (**A**) Representative KAT7 immunofluorescence in WS hMPCs transduced with indicated *KAT7*-targeting sgRNAs at passage 4 (P4) after transduction. White arrows denote cells with reduced KAT7 expression. Data are representative of three independent experiments. Scale bars, 5 μm. (**B**) Growth curve showing the cumulative population doubling of hMPCs transduced with *KAT7*-targeting sgRNAs and their corresponding control sgRNA. $n = 3$ biological replicates. (**C**) Ki67 immunostaining analysis in WS hMPCs transduced with *KAT7*-targeting sgRNAs at P4 after transduction. The white arrows identify Ki67-positive cells. Scale bars, 25 μm. $n = 5$ biological replicates. (**D**) SA-β-gal staining in WS hMPCs transduced with *KAT7*-targeting sgRNAs at P4 after transduction. $n = 5$ biological replicates. (**E**) Heatmap showing reverse transcription quantitative PCR (RT-qPCR) analysis of the indicated genes in WS hMPCs transduced with *KAT7*-targeting sgRNAs at P4 after transduction. Data are representative of two independent experiments. (**F**) Enzyme-linked immunosorbent assay (ELISA) analysis of IL-6 secretion in the culture medium of sg-*KAT7*–transduced WS hMPCs at P4 after transduction. $n = 4$ biological replicates. (**G**) Photon flux quantification of luciferase expression in WS hMPCs transduced with sg-NTCs or sg-*KAT7*#1 and injected into the muscle of nude mice. $n = 5$ mice. (**H**) Quantification of nuclear size in WS hMPCs transduced with *KAT7*-targeting sgRNAs at P4 after transduction. Number of cells ≥ 100, cells from three biological replicates. (**I**) Immunofluorescence analysis of LAP2 expression in WS hMPCs transduced with *KAT7*-targeting sgRNAs at P4 after transduction. White arrows denote cells with decreased LAP2 expression; number of cells ≥ 100, cells from three biological replicates. Scale bars, 25 μm. (**J**) Differential interaction heatmaps for the short arm of chromosome 2 for the indicated conditions in WS hMPCs transduced with sg-NTCs or sg-*KAT7*#1. The color maps are displayed on the same scale for each comparison; red represents enrichment, and blue represents depletion. (**K**) Global switches of A ("active")/B ("inactive") compartments across the genome in WS hMPCs transduced with sg-NTCs or sg-*KAT7*#1. (**L**) Venn diagrams showing differentially expressed genes (DEGs) in both WS hMPCs (relative to WT hMPCs) and sg-*KAT7*#1-transduced WS hMPCs (relative to sg-NTCs-transduced WS hMPCs). (**M**) RNA-seq heatmap comparing genes up-regulated or down-regulated in both WS hMPCs (relative to WT hMPCs) and sg-*KAT7*#1-transduced WS hMPCs (relative to sg-NTCs-transduced WS hMPCs). Representative GO terms are shown to the right. ECM, extracellular matrix. Data are presented as the means ± SEM. Comparisons were performed with one-way ANOVA with Brown-Forsythe test analysis for multiple comparisons and two tailed Student's *t* test [for (G)]. $^{**}P < 0.01$ and $^{***}P < 0.001$.

KAT7 promotes cellular senescence in hMPCs

We next asked whether the ectopic expression of KAT7 was sufficient to promote hMPC senescence. Lentivirus-mediated KAT7 overexpression caused classical features of cellular senescence in young hMPCs, as demonstrated by an increased percentage of SA-β-gal–positive cells (fig. S5A), impaired cell proliferative potential (fig. S5, B to D), induction of aging-associated genes $p16^{INK4A}$ and $p21^{CIP1}$ (fig. S5, E and F), increased SASP with elevated IL-6 secretion (fig. S5G), and an increased DNA damage response (fig. S5H). In addition, KAT7 overexpression resulted in nuclear enlargement and heterochromatin loss with decreased expression of LAP2, Lamin B1, HP1α, and HP1γ (fig. S5, E and F, and summarized in fig. S5, I to L). Collectively, these data establish KAT7 as a potent driver of hMPC senescence.

KAT7 regulates $p15^{INK4b}$ transcription via histone H3 lysine 14 acetylation

KAT7 is reported as a histone acetyltransferase with histone H3 lysine 14 (H3K14) and H3K23 as two known substrates, both positively correlated with transcriptional activation (*26*, *32*). We found that *KAT7* depletion led to reduced H3K14 acetylation (H3K14ac) but not H3K23ac (Fig. 3, A and B, and fig. S6, A to F), indicating that H3K14 is a specific substrate for endogenous KAT7 in hMPCs. Using chromatin immunoprecipitation followed by high-throughput sequencing (ChIP-seq), we found that *KAT7* deficiency down-regulated genome-wide H3K14ac in WS hMPCs, including regions flanking transcriptional start sites (TSSs) (Fig. 3C). Conversely, H3K4 trimethylation (H3K4me3), a control chromatin activation mark, was, in general, not affected by *KAT7* loss in WS hMPCs (fig. S6G). As expected, H3K14ac modifications near TSSs are positively correlated with the magnitude of gene expression (fig. S6H). Integrative analysis of data from H3K14ac ChIP-seq and RNA-seq showed that about one-third of genes (332 of 923) down-regulated upon KAT7 ablation also featured lower H3K14ac in their promoter regions (TSS ± 3 kb) (fig. S6I). Among those genes, 21 were up-regulated upon KAT7 overexpression, which suggests that this gene subset is strongly regulated by the activity of KAT7 in hMPCs (Fig. 3D and fig. S6, I and J). Our data revealed that $p15^{INK4b}$, a cyclin-dependent kinase inhibitor that mediates cell cycle arrest (*33*), was down-regulated upon *KAT7* deficiency and up-regulated by KAT7 overexpression in hMPCs (Fig. 3, D and E).

In our next series of experiments, we explored the mechanistic basis of the *KAT7*-$p15^{INK4b}$ relationship in the hMPC models. We found that *KAT7* depletion abolished the binding of KAT7 around the $p15^{INK4b}$ promoter region and resulted in decreased H3K14ac and $p15^{INK4b}$ expression (Fig. 3F and fig. S6, K to M). Conversely, increased binding of KAT7 to the $p15^{INK4b}$ promoter region by KAT7 overexpression led to higher H3K14ac decoration and $p15^{INK4b}$ transcription (fig. S6, N and O). Ectopic expression of H3K14Q, an H3K14ac-mimic mutant, also up-regulated $p15^{INK4b}$ expression and induced cellular senescence (Fig. 3G and fig. S6, P and Q). In addition, treatment of WS hMPCs with the cell-permeable KAT7 acetyltransferase inhibitor WM-3835 resulted in lower H3K14ac, transcriptional repression of $p15^{INK4b}$, and alleviated cellular senescence (Fig. 3H and fig. S6, R to U) (*27*). Together, these data indicate that *KAT7* modulates $p15^{INK4b}$ expression via H3K14ac in the promoter region.

$p15^{INK4b}$ acts downstream of *KAT7* in mediating senescence

We then investigated the epistatic relationship between *KAT7* and $p15^{INK4b}$ in mediating hMPC senescence. We found that knockout of $p15^{INK4b}$ alleviated the premature senescence of WS hMPCs (fig. S7, A to D), reminiscent of the effects of *KAT7* deficiency, whereas overexpression of $p15^{INK4b}$ promoted hMPC senescence (fig. S7, E to G), phenocopying KAT7 overexpression. Furthermore, $p15^{INK4b}$ overexpression induced cellular senescence, even in *KAT7*-deficient WS and RS hMPCs (Fig. 3, I and J, and fig. S7H). In young hMPCs overexpressing KAT7, $p15^{INK4b}$ depletion was still capable of alleviating premature senescence phenotypes (Fig. 3, I and K, and fig. S7I). Collectively, these data indicate that $p15^{INK4b}$ functions downstream of *KAT7* to reinforce cellular senescence.

The *KAT7*-$p15^{INK4b}$ axis is up-regulated during hMPC aging

We subsequently dissected KAT7 and $p15^{INK4b}$ relationships in different hMPC senescence models. Relative to corresponding WT or younger control cells, we found that the expression of both KAT7 and $p15^{INK4b}$ were increased in WS, HGPS, and RS hMPCs (Fig. 3, L to N, and fig. S8, A and B). Correspondingly, H3K14ac also increased in WS hMPCs (fig. S8C), with increased enrichment of H3K14ac at $p15^{INK4b}$ promoter (fig. S8D). In primary hMPCs derived from aged individuals (79 to 82 years old), we found that KAT7 and $p15^{INK4b}$ protein were elevated compared to those derived from younger counterparts (16 to 28 years old) (Fig. 3O, fig. S8E, and data file S2). However, young primary hMPCs were driven into accelerated cellular senescence by lentivirus-mediated overexpression of KAT7 or $p15^{INK4b}$ (fig. S8F), whereas knockout of either *KAT7* or $p15^{INK4b}$ in aged primary hMPCs delayed the onset of cellular senescence (fig. S8G). These results indicate that the *KAT7*-$p15^{INK4b}$ pathway mediates the pathological and physiological aging of hMPCs.

Gene therapy targeting *KAT7* extends health span and life span in naturally aged mice

Cumulative studies have described how age-associated accumulation of senescent cells in tissues and organs may contribute to the development and progression of aging and aging-related disorders (*1*–*7*, *9*, *10*, *12*). Given the immense therapeutic potential of alleviating aging phenotypes, local rejuvenation of senescent cells by gene therapy or elimination of senescent cells by senolytics is an active research area (*4*, *11*, *24*, *34*). We next investigated whether inactivation of KAT7, which we had demonstrated to counteract senescence in cellular models, could be extended to alleviate features of aging in vivo. To this end, we constructed a lentiviral vector expressing both Cas9 and a mouse sgRNA targeting *Kat7* (or the corresponding controls), which effectively attenuated senescence in primary mouse MPCs (fig. S9, A and B). We then administered lentiviral Cas9/sg-*Kat7* and control vectors intravenously into 20-month aged mice and performed behavioral assays and tissue analysis to evaluate the effects of the intervention (Fig. 4A). Genomic DNA at the *Kat7* locus was specifically targeted in the liver, but not in other tissues (fig. S9C), consistent with the selective enrichment of luminescence in the liver after intravenous injection with an Aka-luciferase reporter lentiviral vector (fig. S9D) (*35*). These results, together with our data showing up-regulation of *Kat7* in the aged mouse liver (fig. S9, E, and F), suggest that the liver may be the main target tissue for the effects of *Kat7* deficiency on organ or individual aging.

Six months after lentiviral Cas9/sg-*Kat7* intervention, we evaluated physiological parameters in the aged mice and found improved overall appearance, grip strength, behavioral response to anxiety, and, most notably, extended life span (Fig. 4, B and C, and fig. S9, G, and H). Treatment with Cas9/sg-*Kat7* not only reduced the numbers

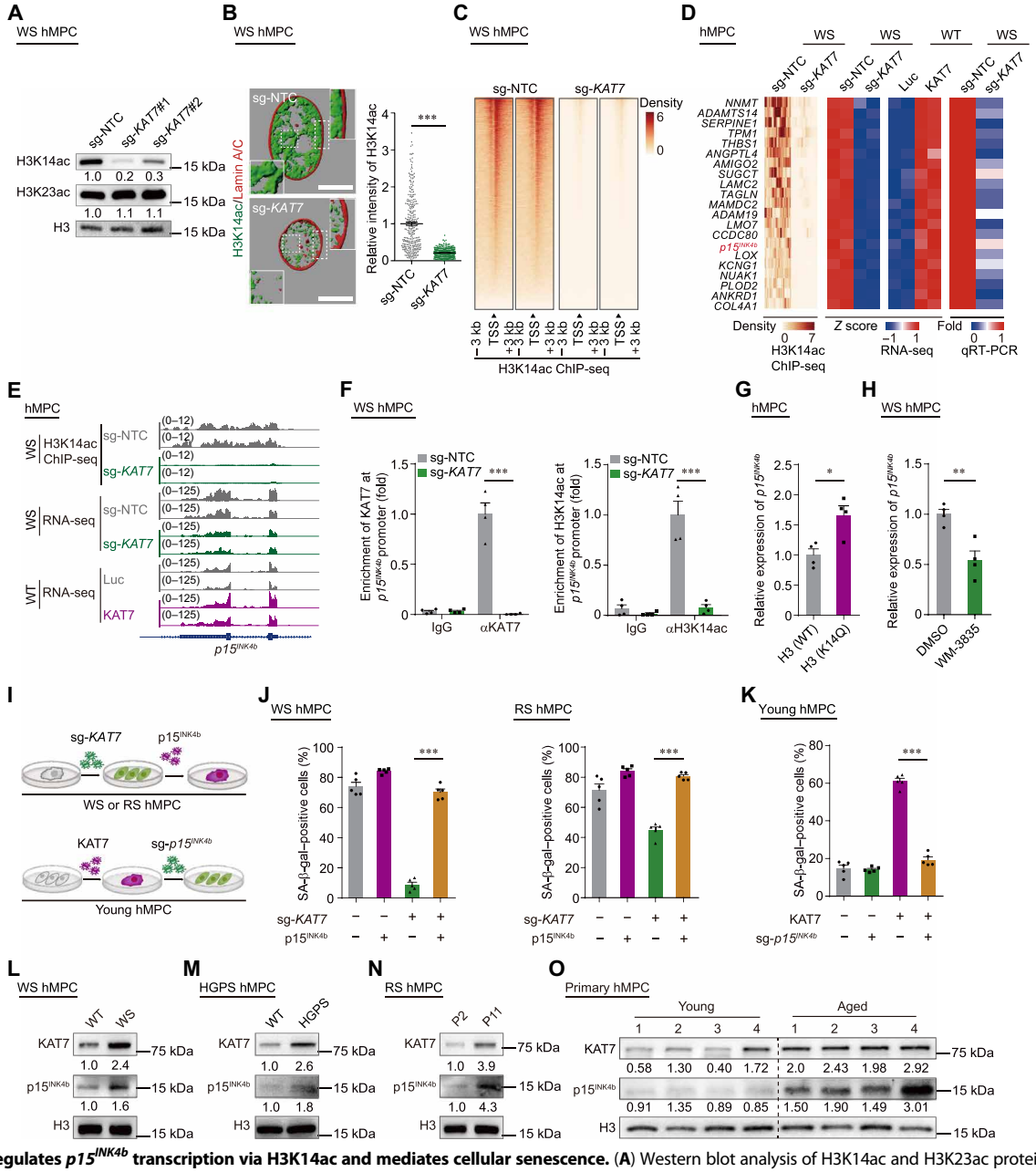

Fig. 3. KAT7 regulates *p15*^{INK4b} transcription via H3K14ac and mediates cellular senescence. (**A**) Western blot analysis of H3K14ac and H3K23ac proteins in WS hMPCs transduced with *KAT7*-targeting sgRNAs at P4 after transduction. Loading control, histone H3. (**B**) Three-dimensional *z*-stack construction of H3K14ac and Lamin A/C immunofluorescence images. Lamin A/C was included for outlining the boundary of the nucleus. Number of cells ≥ 300, cells from three biological replicates. Scale bars, 2 μm. (**C**) Heatmaps showing enrichment of H3K14ac signals surrounding the TSS region (from 3-kb upstream to 3-kb downstream) in sg-*KAT7*#1-transduced WS hMPCs at P4 after transduction. (**D**) Heatmaps showing genes with reduced enrichment of H3K14ac signals surrounding the TSS regions in sg-*KAT7*#1–transduced WS hMPCs, down-regulated and validated by RT-qPCR (data are representative of two independent experiments) in sg-*KAT7*#1–transduced WS hMPCs and increased in KAT7-overexpressing young hMPCs. (**E**) Integrative Genomics Viewer screenshots showing the distribution of H3K14ac mark intensity in the promoter of the *p15*^{INK4b} locus in sg-*KAT7*#1–transduced WS hMPCs, the transcription of *p15*^{INK4b} in sg-*KAT7*#1-transduced WS hMPCs and KAT7-overexpressing young hMPCs. Luc, Luciferase. (**F**) Enrichment of KAT7 (left) and H3K14ac (right) in the promoter of the *p15*^{INK4b} locus in sg-*KAT7*#1–transduced WS hMPCs, as measured by ChIP quantitative PCR at P4 after transduction. $n = 4$ wells per condition. Data are representative of two independent experiments. IgG, immunoglobulin G. (**G**) RT-qPCR analysis of *p15*^{INK4b} expression in H3K14Q-overexpressing hMPCs at P2 after transduction. $n = 4$ wells per condition. Data are representative of two independent experiments. (**H**) RT-qPCR analysis of *p15*^{INK4b} expression in 50 nM WM-3835–treated hMPCs at P4 after treatment. $n = 4$ wells per condition. Data are representative of two independent experiments. DMSO, dimethyl sulfoxide. (**I**) Flow diagram of ectopic expression of *p15*^{INK4b} in sg-*KAT7*#1–transduced WS and RS hMPCs and knockout of *p15*^{INK4b} in KAT7-overexpressing young hMPCs. (**J**) SA-β-gal staining upon ectopic expression of p15^{INK4b} in sg-*KAT7*#1–transduced WS hMPCs at P7 after transduction (left) and RS hMPCs at P5 after transduction (right). $n = 5$ biological replicates. (**K**) SA-β-gal staining in *p15*^{INK4b}-deficient KAT7-overexpressing young hMPCs at P5 after transduction. $n = 5$ biological replicates. (**L** to **N**) Western blot analysis of KAT7 and p15^{INK4b} protein in WS (L), HGPS (M), and RS (N) hMPCs. Loading control, histone H3. (**O**) Western blot analysis of KAT7 and p15^{INK4b} protein in primary hMPCs derived from young and aged healthy individuals. $n = 4$ individuals per group. Loading control, histone H3. Data are presented as the means ± SEM. Comparisons were performed with two tailed Student's *t* test (for G, H) and one-way ANOVA with Brown-Forsythe test analysis for multiple comparisons (for F, J, K). $^*P < 0.05$, $^{**}P < 0.01$, and $^{***}P < 0.001$.

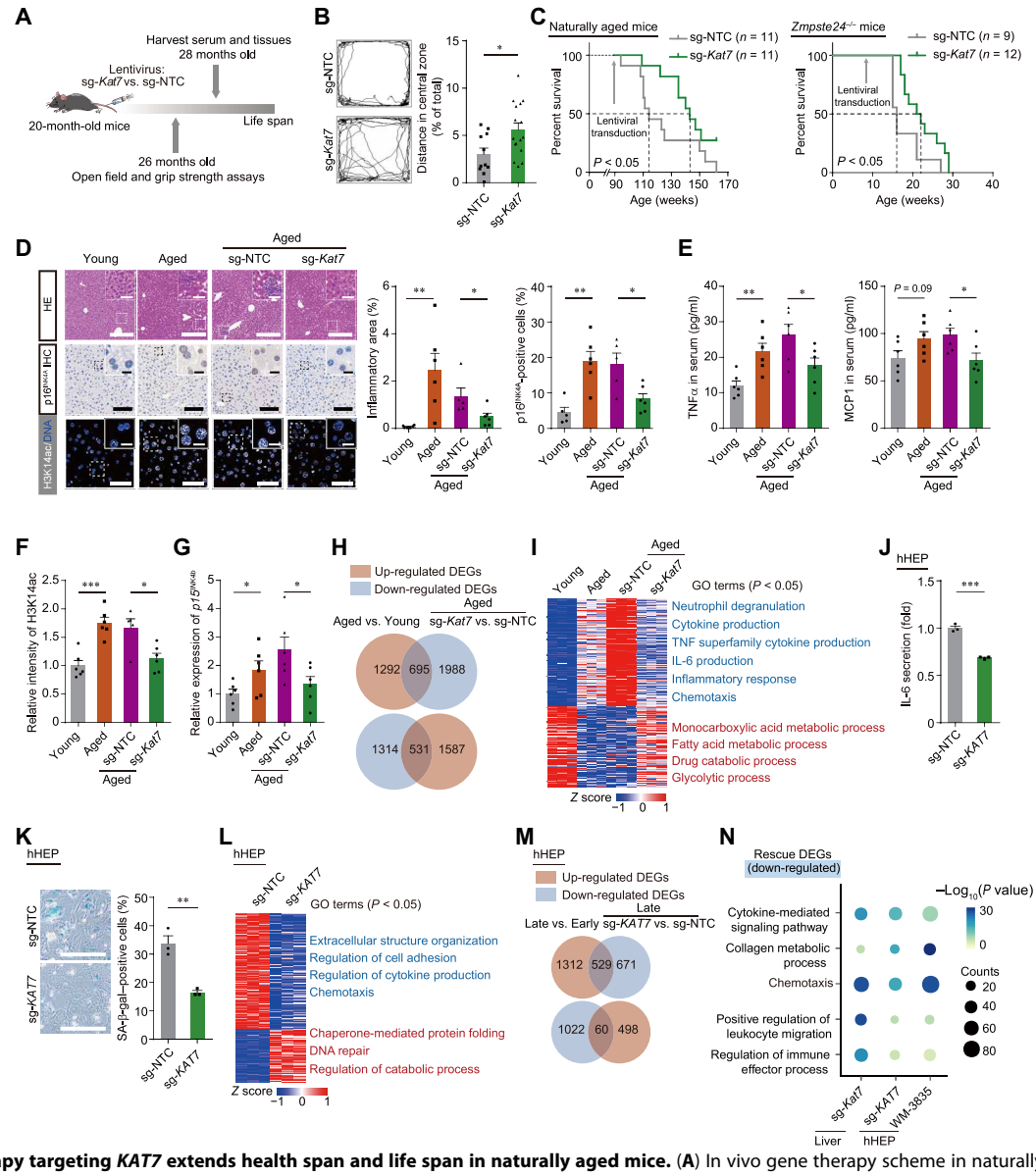

Fig. 4. Gene therapy targeting *KAT7* extends health span and life span in naturally aged mice. (**A**) In vivo gene therapy scheme in naturally aged mice. Twenty-month-old male mice were split into two groups and infected with sg-NTC virus or sg-*Kat7* virus through tail vein injection, assessed by open field test and for grip strength at 26 months, and sampled for serum and tissues at 28 months of age. (**B**) Left: Open-field (OF) test: representative movement traces (black lines) of sg-*Kat7* or sg-NTC virus-infected mice. Right: The normalized distance traveled in the central area of the OF box in sg-NTC ($n = 11$ mice) and in sg-*Kat7* ($n = 16$ mice) virus-infected mice (each mouse was measured twice and the values were averaged). (**C**) Survival curve (left) of naturally aged mice infected with sg-*Kat7* or sg-NTC virus, $n = 11$ mice per group. Survival curve (right) of *Zmpste24*$^{-/-}$ mice infected with sg-*Kat7* or sg-NTC virus through tail vein injection, $n = 9$ or 12 mice per group. (**D**) Hematoxylin and eosin (HE) (top), p16^{INK4A} staining (middle), and H3K14ac staining (bottom) in the liver from young control, 28-month-old control, and 28-month-old mice infected with sg-*Kat7* or sg-NTC virus, respectively. Scale bars, top, 300 μm (zoom: 50 μm), middle, 200 μm (zoom: 50 μm), and bottom, 50 μm (zoom: 12.5 μm), respectively. $n = 5$ to 6 mice per group. IHC, immunohistochemistry. (**E**) TNFα and MCP1 in the serum of 28-month-old mice infected with sg-*Kat7* or sg-NTC virus, $n = 6$ mice per group. (**F**) Quantitative H3K14ac expression data in the liver of 28-month-old mice infected with sg-*Kat7* or sg-NTC virus. $n = 5$ to 6 mice per group. (**G**) RT-qPCR analysis of *p15*^{INK4b} mRNA expression in the liver of 28-month-old mice infected with sg-*Kat7* or sg-NTC virus. $n = 6$ mice per group. (**H**) Venn diagrams showing DEGs in the liver in aged mice (relative to young) and sg-*Kat7*–transduced aged mice (relative to sg-NTC–transduced aged mice). (**I**) RNA-seq heatmap comparing genes up-regulated or down-regulated in the liver of aged versus young and sg-*Kat7* versus sg-NTC-transduced mice. Representative GO terms are shown to the right. (**J**) ELISA analysis of IL-6 in the culture medium of the sg-*KAT7*#1–transduced human primary hepatocytes at late time point. $n = 3$ biological replicates. (**K**) SA-β-gal staining in sg-*KAT7*#1– or sg-NTC–transduced human primary hepatocytes. Scale bars, 100 μm. $n = 3$ biological replicates at late time point. (**L**) RNA-seq heatmap comparing genes up-regulated or down-regulated in sg-*KAT7*#1– versus sg-NTC–transduced human primary hepatocytes. Representative GO terms are shown to the right. (**M**) Venn diagrams showing DEGs in human primary hepatocytes in both late time point (relative to early time point) and sg-*KAT7*#1–transduced human primary hepatocytes (relative to sg-NTC–transduced human primary hepatocytes). (**N**) Representative GO terms and pathways enriched in the rescue DEGs in the mouse liver and human primary hepatocytes after sg-*KAT7* virus infection or 100 nM WM-3835 treatment based on functional enrichment analysis ($P < 0.05$). Dot colors show the statistical significance, and dot size shows the number of genes in the corresponding GO terms. Data are presented as the means ± SEM. Comparisons were performed with two tailed Student's *t* test (for B, J, K) and one-way ANOVA with Brown-Forsythe test analysis for multiple comparisons (for D, E, F, G). Data in (C) were performed with Gehan-Breslow-Wilcoxon test. *$P < 0.05$, **$P < 0.01$, and ***$P < 0.001$.

of $p16^{INK4A}$-positive senescent cells and proinflammatory cells (for example, CD68-positive cells) in the liver but also diminished circulatory SASP factors [MCP1 and tumor necrosis factor–α (TNFα)] (Fig. 4, D and E, and fig. S9I). We next administered the lentiviral Cas9/sg-*Kat7* vector into *Zmpste24*$^{-/-}$ mice, a premature aging model (*36*, *37*) also with increased expression of *Kat7* in the liver (fig. S9, E, and J). Similar to physiologically aged mice, repression of Kat7 expression extended the life span of *Zmpste24*$^{-/-}$ mice (Fig. 4C). We found that *Kat7* depletion led to a reduction of H3K14ac and $p15^{INK4b}$ expression in the mouse liver (Fig. 4, D and F, and summarized in Fig. 4G), consistent with the in vitro results. Together, these results suggest that Kat7 ablation can delay aging in aged mice.

Our genome-wide RNA-seq data revealed that *Kat7* deficiency restored expression of about one-third (1226 of 3832) of DEGs in the livers of aged mice to that of young mice (Fig. 4, H and I, and data file S1), including a panel of known aging-associated genes (from the GenAge database) (fig. S9K) (*38*). The gene ontology (GO) analysis showed that inflammatory response genes were up-regulated during aging and repressed by *Kat7* depletion, such as SASP-related genes *Mmp9*, *Mmp12*, and *Ccl2* (Fig. 4I and fig. S9K). In addition, metabolic pathways such as "monocarboxylic acid metabolism," "fatty acid metabolism" (*Ddah1*), "glycolysis," and "drug catabolic process" (*Cyp2r1*) that were reduced in the aged liver were reactivated by *Kat7* depletion (Fig. 4I and fig. S9L), implying that aging-associated decline in liver metabolic activity could be reversed by Kat7 ablation. In kidney tissues, Cas9/sg-*Kat7*–treated animals exhibited overall fewer DEGs (fig. S9, M and N, and data file S1), but even this, less pronounced shift in gene expression profiles associated with tissue rejuvenation and repressed chronic inflammation was observed (fig. S9, O and P). In all, these data suggest that the down-regulation of *Kat7* is sufficient to alleviate liver senescence and extend the life span in aged mice.

KAT7 depletion alleviates hepatocyte senescence

The ability of *KAT7* to mediate processes underlying mouse liver aging prompted us to investigate *KAT7* as a potential homeostasis regulator in human primary hepatocyte (hHEP) (fig. S10A). We observed that despite being refractory to proliferation, hHEPs underwent progressive cellular senescence in a consecutive in vitro culture system (fig. S10, B to D). Cas9/sgRNA-mediated *KAT7* ablation effectively alleviated senescence parameters in hHEPs, as evidenced by fewer SA-β-gal–positive cells, decreased expression of senescence markers $p15^{INK4b}$ and $p21^{CIP1}$, reduced secretion of pro-inflammatory IL-6, and up-regulated secretion of albumin (ALB), a protein marker of hepatocyte function (Fig. 4, J and K, and fig. S10, E to G). Similarly, the treatment of hHEPs with KAT7 inhibitor WM-3835 resulted in decreased H3K14ac and $p15^{INK4b}$, along with down-regulated IL-6 and up-regulated ALB secretion (fig. S10, B to D and H). Genome-wide RNA-seq results demonstrated that *KAT7* depletion by Cas9/sg-*KAT7* or WM-3835 treatment rescued abnormal gene expression changes in senescent hHEPs (Fig. 4, L and M, fig. S10, I and J, and data file S1). Similar to our findings in the mouse liver, up-regulated genes involved in SASP and compromised expression of metabolic enzymes *CYP1A1*, *CYP7A1*, and *CYP3A1* were reversed upon KAT7 inactivation (fig. S10, K to P). Genes related to cytokine-mediated signaling pathways were commonly rescued in Cas9/sg-*KAT7*–treated hHEPs, WM-3835–treated hHEPs, and Cas9/sg-*Kat7*–treated aged mouse livers (Fig. 4N). In addition, $p15^{INK4b}$ expression in hHEPs was down-regulated upon KAT7 inactivation (fig. S10E), as observed in hMPCs and mouse liver. These results suggest an evolutionarily conservative role of the *KAT7*-$p15^{INK4b}$ pathway in regulating mammalian hepatocyte senescence.

DISCUSSION

We created a systematic CRISPR/Cas9–based genome-wide functional screen to identify genes involved in senescence. Our top hit, the histone acetyltransferase KAT7, catalyzed H3K14ac in the $p15^{INK4b}$ promoter, resulting in increased $p15^{INK4b}$ expression and reinforced cellular senescence. KAT7 ablation alleviated cellular senescence and organ aging and enhanced health span and life span of aged mice, demonstrating the therapeutic potential of KAT7 inactivation in aging-related processes. Much of our understanding of the genetics of aging originates from experiments using short-lived model organisms, such as yeast, worms, flies, and fish (*12*, *39*–*43*). High-throughput RNAi screens in worms have revealed numerous genes that prolong life span when silenced (*39*, *44*). To search for genes controlling cellular senescence in humans, Acosta *et al.* (*14*) screened for short hairpin RNAs (shRNAs) that promote cell proliferation in primary human fibroblasts and identified six candidate genes, including the chemokine receptor *CXCR2* (*IL8RB*), *P53*, and *RB*. Down-regulation of these genes alleviated both replicative senescence and oncogene-induced senescence and reduced the DNA damage response (*14*). Consistent with these results, we also identified a panel of inflammation-related genes such as *C-C chemokine receptor type 5* (*CCR5*) and *NLR family pyrin domain containing 1* (*NLRP1*), the protein initiating inflammasome formation. In addition, Kubben *et al.* (*31*) performed a small interfering RNA (siRNA) screen to assess the involvement of human ubiquitin ligases or their direct modulators in HGPS fibroblasts. Compared to previously used siRNA- or shRNA-based screening tools, pooled CRISPR-Cas9–based knockout screening has improved the specificity and completeness of genetic ablation, thus enabling reliable systematic identification of human aging-related genes and allowing the discovery of targets for aging interventions (*45*). Here, we used the CRISPR-Cas9–based gene knockout strategy, a pooled library of sgRNAs covering the entire annotated human genome, and human stem cell models of premature aging to enable the systematic identification of human aging genes on a genome-wide scale. These efforts markedly expand our understanding of human aging-promoting factors and pave the way toward generating more versatile cell platforms for screening different types of pooled libraries, such as microRNA (miRNA) CRISPR knockout, long noncoding RNA CRISPR knockout, CRISPR interference, and CRISPR transcriptional activation libraries. These tools will be powerful for the high-throughput characterization of human aging/longevity genes and genomic elements.

Enzyme-encoding genes have been shown to regulate aging and life span through epigenetic mechanisms (*40*, *46*–*49*). Histone acetylation is a prominent and reversible epigenetic modification that plays various roles in cellular processes (*13*, *40*, *50*). Previous methods based on shRNA libraries to screen epigenetic regulatory factors related to aging have identified another histone acetyltransferase, *P300*, as a driver for cell aging (*13*). In addition, knockout of *Sir2*, a homolog of the histone deacetylase *SIRT1*, increases H4K16ac and shortens life span in *Saccharomyces cerevisiae* (*40*). Knockout of *SIRT6* in both mice and hMPCs leads to an aging-like phenotype with enriched H3K9ac or H3K56ac (*51*, *52*). Our genome-wide screen showed that the histone acetyltransferase *KAT7* reinforces cellular

senescence, as loss of this gene resulted in decreased H3K14ac and delayed cellular senescence. Although KAT7 has been previously reported as a regulator of prenatal development (*26*, *53*), our study adds a layer of complexity to KAT7 function by revealing its important role in aging biology and pinpointing KAT7 as a new epigenetic target for delaying aging and treating aging-associated disorders. In addition to unraveling the role of KAT7 in mediating aging, our screen identified additional senescence genes that might be targeted to ameliorate aging-related processes. For instance, sgRNA targeting the H3K4 methyltransferase *SETD1B* was also enriched, highlighting the importance of epigenetic regulation of cellular senescence (*41*).

Regarding the physiological relevance of the KAT7 mechanism in aging, we found that lentiviral vector encoding Cas9/sg-*Kat7* alleviated liver senescence and extended health span and life span of mice. Likewise, the administration of *telomerase reverse transcriptase* (*Tert*) delayed various kinds of aging-related diseases and extended the life span of aged mice (*54*–*56*). Recently, it is reported that gene therapy based on three longevity associated genes treated multiple age-related diseases in mice (*57*). Our study adds another example showing the possibility of using gene therapy for antagonizing aging and aging-related disorders. Another screening method based on CRISPR-Cas9 sgRNA identified KAT7 as a target for the treatment of acute myeloid leukemia via the use of its cell-permeable inhibitor WM-3835, suggesting that knockout of *KAT7* inhibits the proliferation of tumor cells, rather than being carcinogenic (*27*). Likewise, in our study, treatment with WM-3835 was found to delay hepatocyte and hMPC senescence, further highlighting the therapeutic potential of KAT7 inhibitor in clinical settings.

Overall, our study highlights the utility of CRISPR-Cas9–based genome-wide screens as innovative tools for uncovering new modulators of cellular senescence that can potentially represent new targets for aging intervention. Nevertheless, our study has several limitations. First, we performed a genome-wide CRISPR-Cas9 screen in hMPCs only and revealed that the loss of KAT7 delayed cellular senescence in hMPCs and hHEPs. Given that the aging mechanism is highly cell type specific, it is necessary to further study the consequences of targeting KAT7 in more cell types or specific organs to define the function and safety scope of *KAT7* intervention. In addition, as a proof of concept, this study used lentivirus as a vector to mediate *Kat7* knockout. In the future, safer delivery vectors such as adenovirus-associated virus may be tested for the safety of *Kat7* intervention in vivo.

MATERIALS AND METHODS

Study design

The goals of this study were (i) to identify new senescence-promoting genes and (ii) to characterize the physiological role of *KAT7* in physiological and pathological aging and highlight the therapeutic potential in treating aging-related diseases. A range of in vitro assays using cell lines such as physiological and pathological aging of hMPCs and hHEPs as well as multiple in vivo assays were performed. For in vitro assays, at least two independent experiments were carried out, and in the case of primary cells, at least two donors were tested. For in vivo mouse studies, age-matched animals were randomly assigned to sg-*Kat7* or sg-NTC treatment groups. Sample sizes were calculated by the investigators on the basis of previous experience. Biochemical and histological outcomes were analyzed with the investigator blinded to the treatment received. Mice were humanely euthanized at defined study end points or reared to the end of life, and all experimental procedures were conducted in compliance with the ethical guidelines of the Institutional Animal Care and Use Committee of the Institute of Zoology, Chinese Academy of Sciences.

Animal experiments

For hMPC transplantation assays, 0.5 million luciferase-expressing hMPCs were injected into the tibialis anterior muscle of nude mice (6 to 8 weeks, male). At days 0 and 3 after transplantation, mice were treated with D-luciferin (GoldBio) and imaged with an IVIS Spectrum imaging system (Xenogen, Caliper). Bioluminescence images were acquired in AUTO mode. For the hMPC tumor susceptibility test, 5 million hMPCs or hESCs suspended in 100 μl of Matrigel/phosphate-buffered saline (PBS) (1:4) were injected into the tibialis anterior muscle of male BALB/c nude mice (6 to 8 weeks) as previously described (*58*).

For lentivirus-targeted organ assays, Aka-luciferase lentivirus was administrated into 6- to 8-week-old male C57BL/6 mice by tail vein injections. After 6 months, mice were treated with AkaLumine-HCl (Sigma-Aldrich) and imaged with an IVIS Spectrum imaging system (Xenogen, Caliper). Bioluminescence images were acquired in AUTO mode.

For the therapeutic physiological aging experiment, male C57BL/6 mice (20 months old) received lentiviral Cas9/sg-*Kat7* by intravenous injection. Six mice per group were humanely euthanized and harvested tissues and blood at 28 months old, and others were reared to the end of life. For the therapeutic pathological aging experiment, male *Zmpste24*$^{-/-}$ mice (around 8 weeks old) received lentiviral Cas9/sg-*Kat7* by intravenous injection and were reared to the end of life.

Generation and genotyping of *Zmpste24*$^{-/-}$ mice

CRISPR-Cas9–mediated gene targeting was performed using previously described methods, with some modifications (*59*). To generate *Zmpste24*$^{-/-}$ mice, we deleted exon 2 to exon 6 using two sgRNAs (data file S2) targeting the intron 1 and intron 6 of the *Zmpste24* gene and resulting in a 646–base pair deletion in the coding sequence. Then, 230 zygotes were selected for intracytoplasmic injection and transferred into the surrogate mothers. The construction of *Zmpste24*$^{-/-}$ mice was performed by Beijing Vital River Laboratory Animal Technology Co. Ltd., and genomic DNA was extracted from tail tissues. The targeted fragments were amplified using EasyTaq polymerase (TaKaRa) with the primers shown in data file S2.

Cell culture

The procedure to differentiate WT (WiCell Research, H9 hESC line), WS, and HGPS embryonic stem cell lines (genetically edited H9 ESC with disease-specific mutation) into MPCs was as described previously (*18*, *19*). Briefly, 10 to 15 embryoid bodies were plated on Matrigel (BD Biosciences)–coated six-well plates in minimum essential medium–α (MEM-α) medium (Thermo Fisher Scientific) supplemented with 10% fetal bovine serum (FBS; Gemcell), 1% NEAA (nonessential amino acid) (Thermo Fisher Scientific), 1% penicillin/streptomycin (Thermo Fisher Scientific), as well as fibroblast growth factor 2 (FGF2) (10 ng/ml) (Joint Protein Central, JPC) and transforming growth factor–β (5 ng/ml) (Humanzyme). Cells were cultured for another 10 days until MPC-like populations occurred. The resulting cells were analyzed and purified by fluorescence-activated

cell sorting (FACS) using antibodies corresponding to the MPC signature, including anti-CD73 (BD Biosciences, 550741), anti-CD90 (BD Biosciences, 555595), and anti-CD105 (eBioscience, 17-1057). To demonstrate MPC identity, Von Kossa, Oil Red O, and toluidine blue staining were conducted to evaluate the osteogenic, adipogenic, and chondrogenic potential of MPC as previously reported (*18*, *19*). Human primary MPCs (derived from gingival samples) were separated from gingival samples as previously described (*18*). Briefly, gingival samples from young and aged donors were rinsed twice with cold PBS (Sigma-Aldrich) and then resuspended with 1 ml of TrypLE (Thermo Fisher Scientific) [containing Dispase (2 mg/ml; Sigma-Aldrich)] at 37°C for 30 min. Dissociated cells and gingival samples were centrifuged at 1000 rpm/min for 5 min and then cultured in MEM-α medium (Thermo Fisher Scientific) supplemented with 10% FBS (Gemcell), 1% NEAA (Thermo Fisher Scientific), 1% penicillin/streptomycin (Thermo Fisher Scientific), and FGF2 (1 ng/ml) (JPC) until MPC-like populations occurred from gingival samples. WT, WS, HGPS (derived from H9 ESC), and human primary MPCs (derived from gingival samples) were maintained in MEM-α medium (Thermo Fisher Scientific) supplemented with 10% FBS (Gemcell), 1% NEAA (Thermo Fisher Scientific), 1% penicillin/streptomycin (Thermo Fisher Scientific), and FGF2 (1 ng/ml) (JPC). Human embryonic kidney (HEK) 293T cells were maintained in high-glucose Dulbecco's modified Eagle's medium containing 10% FBS (Gemcell) and 1% penicillin/streptomycin (Thermo Fisher Scientific). hHEPs (Lonza, HUCPI) were maintained in culture medium (Lonza, CC-3198). No mycoplasma contamination was detected during cell culture.

CRISPR-Cas9–based library screen

Lentivirus transduction

GeCKOv2 was purchased from Addgene (version A: 1000000048 and version B: 1000000049) and applied in all CRISPR-Cas9 screens. Versions A and B, containing four unique constructs per miRNA and six per protein-coding gene as well as 1000 control sgRNAs (no effect) (used for evaluating the enrichment for candidate hits), were pooled and used for the screens. The GeCKOv2 library screen was performed as described previously (*60*). Briefly, viruses were harvested from HEK293T cells transfected with the GeCKOv2 library plasmid or six control sgRNAs (randomly chosen from the 1000 control sgRNAs and used for all the phenotypic analyses) with pMD2G and psPAX2 using Lipofectamine 3000 transfection reagent (Thermo Fisher Scientific), concentrated, and titrated. WS hMPCs were transfected with the GeCKOv2 library at a calculated multiplicity of infection (MOI) of 0.3 to 0.4 with an expected library coverage of 100× per individual infection, with polybrene (8 μg/ml) (Thermo Fisher Scientific) for 16 hours at 37°C. Three days after infection, cells were treated with puromycin (1 μg/ml) (InvivoGen) for 7 days and puromycin (0.5 μg/ml) for 14 days for positive selection. Cells were then cultured for another 32 days to allow rejuvenated WS hMPCs to become dominant. Fresh medium was added every other day, and cells were expanded in additional plates to maintain appropriate confluency. More than 10 million cells were maintained during the CRISPR-Cas9 screening process to prevent loss of constructs with low initial counts or overrepresentation of constructs with high initial counts. Genomic DNA was extracted from harvested cells at 4 and 6 weeks after infection, and at the end of the experiment (8 weeks), using a QIAGEN DNeasy blood and tissue kit. The genomic DNA extracted at the mid-experiment and final time points was sequenced to evaluate library representation, and the initial point was assessed by plasmid sequencing.

Polymerase chain reaction detection of lentiCRISPRv2 constructs

Polymerase chain reaction (PCR) was performed on genomic DNA using PrimerSTAR HS DNA Polymerase following the manufacturer's instructions (TaKaRa). A two-step PCR method was used to amplify inserted sgRNA sequences and the appended molecular barcodes and Illumina adapter sequences (*60*). Primers (data file S2) flanking the sgRNA sequences were designed with a biotinylated forward primer for the first step. The reaction conditions were as follows: (i) denaturation at 98°C for 2 min; (ii) 14 cycles at 98°C for 10 s, annealing at 58°C for 30 s, and extension at 72°C for 40 s; and (iii) a final single extension step at 72°C for 5 min. More than 75 reactions (2 μg of genomic DNA per reaction) per library were performed to ensure adequate input library coverage. The amplicons were then combined and purified with C1 beads (Thermo Fisher Scientific) and used as a template for the second PCR step. The primers used in the second PCR step were appended with the Illumina HiSeq 2500 adapter and barcode sequences. The reaction conditions were the same as those for the first PCR step except that only 12 cycles were used.

Computational analysis of sequencing data from CRISPR-Cas9 experiments

Clean reads were obtained by filtering raw CRISPR-Cas9 sequencing data to remove adapter sequences and low-quality bases with custom scripts, and sequencing data were then analyzed with Model-based Analysis of Genome-wide CRISPR-Cas9 Knockout (MAGeCK) (version 0.5.7). Read counts were initially obtained from individual samples with the count command in MAGeCK, in which the software fastqc was used to assess the quality of the sequencing data, and reads from high-quality samples were further mapped to the screening library. The top positively selected and negatively selected sgRNAs were identified with the test command in MAGeCK, and in this process, read counts were normalized on the basis of total count normalization to exclude the effect of sequencing depth (*61*). The robust rank aggregation (α-RRA) algorithm was then used to calculate the RRA score, which reflects the degree of positive or negative selection.

Clustering sgRNAs based on the abundance

The sgRNA abundance $sgRNAs_{i,j}$ (in million) for sgRNA *i* in sample *j* was calculated by dividing the sgRNA count for sgRNA *i* by the sum of sgRNA counts in sample *j*. According to the dynamic changes of sgRNAs at different time points, all sgRNAs were separated into two groups: group 1 with sgRNA whose abundance decreased from the baseline along the time and group 2 with the other sgRNA. To cluster sgRNAs in either group with different patterns based on the sgRNA abundance, the function genesCluster (parameter "k = 10") in the R package cummeRbund based on the $\log_2$-transferred fold change between the sample *j* and the baseline. GO analysis was performed with Metascape with default parameters.

Genetic interaction network

For cells collected at 4, 6, or 8 weeks after infection, top-ranked 500 positive selection genes with at least one sgRNA were individually used to perform the protein-protein interaction enrichment analysis based on website tool Metascape and visualized the interaction network using software Cytoscape (*62*).

ChIP-seq library preparation and sequencing

Cells were cross-linked with 1% (v/v) formaldehyde for 8 to 12 min at room temperature (RT). For acetylated histone ChIP, an additional 20 mM sodium butyrate was included. Samples were then resuspended in ice-cold lysis buffer [50 mM Tris-HCl, 10 mM EDTA, and 1% SDS (pH 8.0)] for 5 min, followed by chromatin shearing using a Covaris S2 instrument. The fragmented chromatin was incubated overnight at 4°C with protein A beads conjugated to 2.4 μg of the following primary antibodies: anti-H3K4me3 (Abcam, ab8580) and anti-H3K14ac (Millipore, 07-353). Normal rabbit immunoglobulin G (Cell Signaling Technology, #2729S) or fragmented chromatin input was used as the control. Immunoprecipitated chromatin was eluted in elution buffer and decross-linked at 68°C for 2 hours with proteinase K on a thermomixer. DNA was then isolated using phenol-chloroform-isoamyl alcohol extraction and ethanol precipitation. Purified DNA was used to construct a sequencing library with the KAPA Hyper Preparation Kit (Kapa biosystems) according to the manufacturer's instructions.

ChIP-seq data processing

Clean reads, obtained by removing adapter sequences from the raw ChIP-seq data with custom scripts, were mapped to the reference genome [University of California, Santa Cruz (UCSC) human hg19 or the custom-combined reference genome] using Bowtie2 (version 2.2.3) with default parameters.

For H3K14ac, clean reads were mapped to the custom-combined reference genome, which was concatenated with the human (UCSC hg19) and *Drosophila* (UCSC dm6) genomes, as previously reported (*63*). To build the combined reference genome, we labeled chromosome names in the *Drosophila* reference genome with the '_dm6' suffix so that we can easily separate the reads mapped into the human or *Drosophila* furtherly. A custom alignment library was built for the combined reference with Bowtie2. After the mapping process, only uniquely mapped nonduplicate reads were retained with MACS2 (version 2.1.1.20160309). To quantify the ChIP-seq signal, a normalization factor was used as previously reported (*63*). Briefly, we defined α as the normalization factor, β as the signal from the *Drosophila* cells, *Nd* as the number of reads (in millions) uniquely mapped to the *Drosophila* reference genome and *r* as the percentage of *Drosophila* cells. Therefore, the formula was defined as follows

$$\beta = \alpha \times \frac{Nd}{\gamma}$$

Because the signal from *Drosophila* cells β and the percentage of *Drosophila* cells *r* was constant across samples, we simplified these values to β = 1 and *r* = 1. Accordingly, the normalization factor was defined as follows

$$\alpha = 1/Nd$$

The ChIP-seq signals were normalized to the normalization factor and visualized with software deepTools.

For H3K4me3, we directly mapped the ChIP-seq data to the human genome hg19 and normalized the ChIP-seq signals to the number of reads uniquely mapped to the human reference genome.

ChIP-seq peaks calling

For calling the H3K14ac ChIP-seq peaks, we merged the ChIP-seq signal files corresponding to sg-NTC, sg-*KAT7*, and input files. We predicted the fragment size with predictd command in MACS2 and then called peaks with callpeak command in MACS2 (parameters "-g 2.7e9 --keep-dup all --nomodel --extsize 306 --broad --broad-cutoff 0.05") to lastly obtain 39,103 peaks. We then used multiBigwigSummary BED-file command in deepTools to calculate the ChIP-seq peak scores and defined peaks with a fold change of more than 3 between H3K14ac sg-NTC and H3K14ac sg-*KAT7* as different peaks (39,018 peaks).

Lentivirus preparation and titration

To construct lentiviral vectors expressing sgRNA targeting *KAT7* or $p15^{INK4b}$, sg-NTC, or other sgRNA, corresponding sgRNA oligonucleotides (data file S2) were inserted into the cloning site of lentiCRISPRv2 (Addgene, #52961) following the manufacturer's instructions. To construct lentiviral vectors expressing shRNA targeting *KAT7*, the corresponding shRNA oligonucleotides (data file S2) were inserted into the cloning site of pLVTHM (Addgene, #12247), digested by the restriction endonucleases Cla I and Mlu I. To construct lentiviral vectors expressing FLAG-KAT7, FLAG-H3 (K14Q), and FLAG-$p15^{INK4b}$, the corresponding complementary DNAs (cDNAs) were amplified by PCR and cloned into the pLE4 lentiviral vector (a gift from T. Hishida). For lentiviral vector encoding Aka-luciferase, the corresponding DNA was amplified by PCR from pcDNA3 venus-Akaluc (RDB15781) (*35*) and cloned into the pLE4 lentiviral vector. Lentivirus was packaged with pMD2G and psPAX2 using Lipofectamine 3000 transfection reagent (Thermo Fisher Scientific) in HEK 293T. For virus titration, sgRNA viruses were tested by counting the cell clones after puromycin selection, and shRNA or overexpression viruses were tested by GFP fluorescence or immunostaining for Flag, respectively.

SA-β-gal staining

Cultured cells were washed with PBS and fixed in a solution containing 2% formaldehyde and 0.2% glutaraldehyde at RT for 5 min. Fixed cells were stained with fresh staining solution containing X-gal (5-bromo-4-chloro-3-indolyl β-D-galactopyranoside) to measure SA-β-gal activity at 37°C overnight. Images were taken and the percentages of positive cells were calculated and analyzed using ImageJ; except in Fig. 1D, the percentages of negative cells were calculated and analyzed.

Immunofluorescence staining

Cells and tissue sections were fixed in 4% paraformaldehyde (PFA) in PBS at RT for 20 min and were then permeabilized with 0.4% Triton X-100 in PBS at RT for 30 min after washing with PBS. Cells were then blocked with 10% donkey serum (Jackson ImmunoResearch Laboratories) for 1 hour and incubated with primary antibodies at 4°C for 16 hours, primary antibodies were anti-H3K14ac (07-353) and anti-H3K23ac (07-355) from Millipore and anti-KAT7 (ab70183), and anti-CD68 (ab125212) from Abcam, followed by incubation with the corresponding secondary antibodies (Thermo Fisher Scientific) and Hoechst 33342 (Thermo Fisher Scientific; 5 μg/ml) at RT for 1 hour. A Leica SP5 confocal microscope was used for imaging.

Histology analysis

Tissues were fixed at 4°C with 4% PFA for 1 week and then embedded in paraffin. Five-micrometer sections were stained with hematoxylin and eosin (HE) and Sirius Red according to the manufacturer's protocol.

Immunohistochemistry

Immunohistochemistry was performed using a heat-mediated antigen retrieval procedure and by blocking endogenous peroxidases with hydrogen peroxide. Tissue sections were then incubated with a primary antibody overnight at 4°C and incubated with the appropriate secondary antibody (ZSGB-Biotech) for 30 min. Visualization was performed using a diaminobenzidine substrate kit (ZSGB-Biotech) according to the manufacturer's instructions. Anti-$p16^{INK4A}$ antibody (Abcam, ab54210) and anti-KAT7 antibody (Cell Signaling Technology, #58418) were used as the primary antibodies.

Statistical analysis

Statistical analyses were performed using Prism version 6 software (GraphPad Software). Data are presented as means ± SEM. Comparisons were performed with Student's *t* test or one-way analysis of variance (ANOVA) with Brown-Forsythe test for multiple comparisons. $P < 0.05$ was defined as statistically significant.

SUPPLEMENTARY MATERIALS

stm.sciencemag.org/cgi/content/full/13/575/eabd2655/DC1
Materials and Methods
Fig. S1. A genome-wide CRISPR-Cas9–based screen for senescence-promoting genes in hMPCs.
Fig. S2. *KAT7* knockdown reverses the premature aging phenotypes of WS hMPCs.
Fig. S3. *KAT7* regulates both physiological and pathological cellular aging.
Fig. S4. *KAT7* regulates cellular senescence induced by different stressors.
Fig. S5. *KAT7* promotes cellular senescence in early-passage hMPCs.
Fig. S6. *KAT7* regulates cellular senescence via acetylation of H3K14 and subsequent upregulation of $p15^{INK4b}$.
Fig. S7. $p15^{INK4b}$ regulates cellular senescence in hMPCs.
Fig. S8. Expression of *KAT7* and $p15^{INK4b}$ increases with age.
Fig. S9. *KAT7* regulates individual life span in mice.
Fig. S10. Knockout of *KAT7* alleviates hepatocyte senescence.
Data file S1. TOP 100 ranked genes in the genome-wide CRISPR-based screen and DEGs of RNA-seq (Excel).
Data file S2. Primer and antibody information as well as donor information (Excel).
Data file S3. Raw data (Excel).

View/request a protocol for this paper from *Bio-protocol*.

REFERENCES AND NOTES

1. J. M. van Deursen, The role of senescent cells in ageing. *Nature* **509**, 439–446 (2014).
2. J. Campisi, Aging, cellular senescence, and cancer. *Annu. Rev. Physiol.* **75**, 685–705 (2013).
3. M. Ogrodnik, S. Miwa, T. Tchkonia, D. Tiniakos, C. L. Wilson, A. Lahat, C. P. Day, A. Burt, A. Palmer, Q. M. Anstee, S. N. Grellscheid, J. H. J. Hoeijmakers, S. Barnhoorn, D. A. Mann, T. G. Bird, W. P. Vermeij, J. L. Kirkland, J. F. Passos, T. von Zglinicki, D. Jurk, Cellular senescence drives age-dependent hepatic steatosis. *Nat. Commun.* **8**, 15691 (2017).
4. A. M. Papatheodoridi, L. Chrysavgis, M. Koutsilieris, A. Chatzigeorgiou, The role of senescence in the development of nonalcoholic fatty liver disease and progression to nonalcoholic steatohepatitis. *Hepatology* **71**, 363–374 (2020).
5. C. Lopez-Otin, M. A. Blasco, L. Partridge, M. Serrano, G. Kroemer, The hallmarks of aging. *Cell* **153**, 1194–1217 (2013).
6. D. J. Baker, B. G. Childs, M. Durik, M. E. Wijers, C. J. Sieben, J. Zhong, R. A. Saltness, K. B. Jeganathan, G. C. Verzosa, A. Pezeshki, K. Khazaie, J. D. Miller, J. M. van Deursen, Naturally occurring p16(Ink4a)-positive cells shorten healthy lifespan. *Nature* **530**, 184–189 (2016).
7. S. He, N. E. Sharpless, Senescence in health and disease. *Cell* **169**, 1000–1011 (2017).
8. U. Herbig, M. Ferreira, L. Condel, D. Carey, J. M. Sedivy, Cellular senescence in aging primates. *Science* **311**, 1257 (2006).
9. J. C. Jeyapalan, J. M. Sedivy, Cellular senescence and organismal aging. *Mech. Ageing Dev.* **129**, 467–474 (2008).
10. O. Karin, A. Agrawal, Z. Porat, V. Krizhanovsky, U. Alon, Senescent cell turnover slows with age providing an explanation for the Gompertz law. *Nat. Commun.* **10**, 5495 (2019).
11. D. J. Baker, T. Wijshake, T. Tchkonia, N. K. LeBrasseur, B. G. Childs, B. van de Sluis, J. L. Kirkland, J. M. van Deursen, Clearance of p16Ink4a-positive senescent cells delays ageing-associated disorders. *Nature* **479**, 232–236 (2011).
12. P. P. Singh, B. A. Demmitt, R. D. Nath, A. Brunet, The genetics of aging: A vertebrate perspective. *Cell* **177**, 200–220 (2019).
13. P. Sen, Y. Lan, C. Y. Li, S. Sidoli, G. Donahue, Z. Dou, B. Frederick, Q. Chen, L. J. Luense, B. A. Garcia, W. Dang, F. B. Johnson, P. D. Adams, D. C. Schultz, S. L. Berger, Histone acetyltransferase p300 induces de novo super-enhancers to drive cellular senescence. *Mol. Cell* **73**, 684–698.e8 (2019).
14. J. C. Acosta, A. O'Loghlen, A. Banito, M. V. Guijarro, A. Augert, S. Raguz, M. Fumagalli, M. Da Costa, C. Brown, N. Popov, Y. Takatsu, J. Melamed, F. d'Adda di Fagagna, D. Bernard, E. Hernando, J. Gil, Chemokine signaling via the CXCR2 receptor reinforces senescence. *Cell* **133**, 1006–1018 (2008).
15. Z. Zou, X. Long, Q. Zhao, Y. Zheng, M. Song, S. Ma, Y. Jing, S. Wang, Y. He, C. R. Esteban, N. Yu, J. Huang, P. Chan, T. Chen, J. C. Izpisua Belmonte, W. Zhang, J. Qu, G. H. Liu, A single-cell transcriptomic atlas of human skin aging. *Dev. Cell* (2020).
16. D. W. Morgens, R. M. Deans, A. Li, M. C. Bassik, Systematic comparison of CRISPR/Cas9 and RNAi screens for essential genes. *Nat. Biotechnol.* **34**, 634–636 (2016).
17. J. D. Sander, J. K. Joung, CRISPR-Cas systems for editing, regulating and targeting genomes. *Nat. Biotechnol.* **32**, 347–355 (2014).
18. W. Zhang, J. Li, K. Suzuki, J. Qu, P. Wang, J. Zhou, X. Liu, R. Ren, X. Xu, A. Ocampo, T. Yuan, J. Yang, Y. Li, L. Shi, D. Guan, H. Pan, S. Duan, Z. Ding, M. Li, F. Yi, R. Bai, Y. Wang, C. Chen, F. Yang, X. Li, Z. Wang, E. Aizawa, A. Goebl, R. D. Soligalla, P. Reddy, C. R. Esteban, F. Tang, G.-H. Liu, J. C. Belmonte, Aging stem cells. A Werner syndrome stem cell model unveils heterochromatin alterations as a driver of human aging. *Science* **348**, 1160–1163 (2015).
19. Z. Wu, W. Zhang, M. Song, W. Wang, G. Wei, W. Li, J. Lei, Y. Huang, Y. Sang, P. Chan, C. Chen, J. Qu, K. Suzuki, J. C. I. Belmonte, G. H. Liu, Differential stem cell aging kinetics in Hutchinson-Gilford progeria syndrome and Werner syndrome. *Protein Cell* **9**, 333–350 (2018).
20. N. E. Sanjana, O. Shalem, F. Zhang, Improved vectors and genome-wide libraries for CRISPR screening. *Nat. Methods* **11**, 783–784 (2014).
21. G. Korkmaz, R. Lopes, A. P. Ugalde, E. Nevedomskaya, R. Han, K. Myacheva, W. Zwart, R. Elkon, R. Agami, Functional genetic screens for enhancer elements in the human genome using CRISPR-Cas9. *Nat. Biotechnol.* **34**, 192–198 (2016).
22. A. Chojnowski, P. F. Ong, O. Dreesen, Nuclear lamina remodelling and its implications for human disease. *Cell Tissue Res.* **360**, 621–631 (2015).
23. N. J. Ullrich, L. B. Gordon, Hutchinson-Gilford Progeria Syndrome. *Handb. Clin. Neurol.* **132**, 249–264 (2015).
24. C. Liang, Z. Liu, M. Song, W. Li, Z. Wu, Z. Wang, Q. Wang, S. Wang, K. Yan, L. Sun, T. Hishida, Y. Cai, J. C. I. Belmonte, P. Guillen, P. Chan, Q. Zhou, W. Zhang, J. Qu, G. H. Liu, Stabilization of heterochromatin by CLOCK promotes stem cell rejuvenation and cartilage regeneration. *Cell Res.* 10.1038/s41422-020-0385-7 (2020).
25. N. Kubben, T. Misteli, Shared molecular and cellular mechanisms of premature ageing and ageing-associated diseases. *Nat. Rev. Mol. Cell Biol.* **18**, 595–609 (2017).
26. A. J. Kueh, M. P. Dixon, A. K. Voss, T. Thomas, HBO1 is required for H3K14 acetylation and normal transcriptional activity during embryonic development. *Mol. Cell. Biol.* **31**, 845–860 (2011).
27. L. MacPherson, J. Anokye, M. M. Yeung, E. Y. N. Lam, Y. C. Chan, C. F. Weng, P. Yeh, K. Knezevic, M. S. Butler, A. Hoegl, K. L. Chan, M. L. Burr, L. J. Gearing, T. Willson, J. Liu, J. Choi, Y. Yang, R. A. Bilardi, H. Falk, N. Nguyen, P. A. Stupple, T. S. Peat, M. Zhang, M. de Silva, C. Carrasco-Pozo, V. M. Avery, P. S. Khoo, O. Dolezal, M. L. Dennis, S. Nuttall, R. Surjadi, J. Newman, B. Ren, D. J. Leaver, Y. Sun, J. B. Baell, O. Dovey, G. S. Vassiliou, F. Grebien, S. J. Dawson, I. P. Street, B. J. Monahan, C. J. Burns, C. Choudhary, M. E. Blewitt, A. K. Voss, T. Thomas, M. A. Dawson, HBO1 is required for the maintenance of leukaemia stem cells. *Nature* **577**, 266–270 (2020).
28. Z. Chen, L. Zhou, L. Wang, G. Kazobinka, X. Zhang, X. Han, B. Li, T. Hou, HBO1 promotes cell proliferation in bladder cancer via activation of Wnt/β-catenin signaling. *Mol. Carcinog.* **57**, 12–21 (2018).
29. A. Zirkel, M. Nikolic, K. Sofiadis, J. P. Mallm, C. A. Brackley, H. Gothe, O. Drechsel, C. Becker, J. Altmuller, N. Josipovic, T. Georgomanolis, L. Brant, J. Franzen, M. Koker, E. G. Gusmao, I. G. Costa, R. T. Ullrich, W. Wagner, V. Roukos, P. Nurnberg, D. Marenduzzo, K. Rippe, A. Papantonis, HMGB2 loss upon senescence entry disrupts genomic organization and induces CTCF clustering across cell types. *Mol. Cell* **70**, 730–744.e6 (2018).
30. S. W. Criscione, M. De Cecco, B. Siranosian, Y. Zhang, J. A. Kreiling, J. M. Sedivy, N. Neretti, Reorganization of chromosome architecture in replicative cellular senescence. *Sci. Adv.* **2**, e1500882 (2016).
31. N. Kubben, W. Zhang, L. Wang, T. C. Voss, J. Yang, J. Qu, G. H. Liu, T. Misteli, Repression of the antioxidant NRF2 pathway in premature aging. *Cell* **165**, 1361–1374 (2016).
32. A. Zippo, R. Serafini, M. Rocchigiani, S. Pennacchini, A. Krepelova, S. Oliviero, Histone crosstalk between H3S10ph and H4K16ac generates a histone code that mediates transcription elongation. *Cell* **138**, 1122–1136 (2009).
33. F. Wang, L. Zhang, p15(INK4b) regulates cell cycle signaling in hippocampal astrocytes of aged rats. *Aging Clin. Exp. Res.* **28**, 813–821 (2016).
34. Y. Cai, H. Zhou, Y. Zhu, Q. Sun, Y. Ji, A. Xue, Y. Wang, W. Chen, X. Yu, L. Wang, H. Chen, C. Li, T. Luo, H. Deng, Elimination of senescent cells by β-galactosidase-targeted prodrug attenuates inflammation and restores physical function in aged mice. *Cell Res.* **30**, 574–589 (2020).

35. S. Iwano, M. Sugiyama, H. Hama, A. Watakabe, N. Hasegawa, T. Kuchimaru, K. Z. Tanaka, M. Takahashi, Y. Ishida, J. Hata, S. Shimozono, K. Namiki, T. Fukano, M. Kiyama, H. Okano, S. Kizaka-Kondoh, T. J. McHugh, T. Yamamori, H. Hioki, S. Maki, A. Miyawaki, Single-cell bioluminescence imaging of deep tissue in freely moving animals. *Science* **359**, 935–939 (2018).
36. J. Barrowman, S. Michaelis, ZMPSTE24, an integral membrane zinc metalloprotease with a connection to progeroid disorders. *Biol. Chem.* **390**, 761–773 (2009).
37. G. Marino, A. P. Ugalde, A. F. Fernandez, F. G. Osorio, A. Fueyo, J. M. Freije, C. Lopez-Otin, Insulin-like growth factor 1 treatment extends longevity in a mouse model of human premature aging by restoring somatotroph axis function. *Proc. Natl. Acad. Sci. U.S.A.* **107**, 16268–16273 (2010).
38. R. Tacutu, D. Thornton, E. Johnson, A. Budovsky, D. Barardo, T. Craig, E. Diana, G. Lehmann, D. Toren, J. Wang, V. E. Fraifeld, J. P. de Magalhaes, Human ageing genomic resources: New and updated databases. *Nucleic Acids Res.* **46**, D1083–D1090 (2018).
39. B. Hamilton, Y. Dong, M. Shindo, W. Liu, I. Odell, G. Ruvkun, S. S. Lee, A systematic RNAi screen for longevity genes in *C. elegans*. *Genes Dev.* **19**, 1544–1555 (2005).
40. W. Dang, K. K. Steffen, R. Perry, J. A. Dorsey, F. B. Johnson, A. Shilatifard, M. Kaeberlein, B. K. Kennedy, S. L. Berger, Histone H4 lysine 16 acetylation regulates cellular lifespan. *Nature* **459**, 802–807 (2009).
41. S. Han, E. A. Schroeder, C. G. Silva-Garcia, K. Hebestreit, W. B. Mair, A. Brunet, Mono-unsaturated fatty acids link H3K4me3 modifiers to *C. elegans* lifespan. *Nature* **544**, 185–190 (2017).
42. J. Feng, F. Bussiere, S. Hekimi, Mitochondrial electron transport is a key determinant of life span in *Caenorhabditis elegans*. *Dev. Cell* **1**, 633–644 (2001).
43. M. Uno, E. Nishida, Lifespan-regulating genes in *C. elegans*. *NPJ Aging Mech Dis* **2**, 16010 (2016).
44. M. Hansen, A. L. Hsu, A. Dillin, C. Kenyon, New genes tied to endocrine, metabolic, and dietary regulation of lifespan from a *Caenorhabditis elegans* genomic RNAi screen. *PLOS Genet.* **1**, 119–128 (2005).
45. B. Evers, K. Jastrzebski, J. P. Heijmans, W. Grernrum, R. L. Beijersbergen, R. Bernards, CRISPR knockout screening outperforms shRNA and CRISPRi in identifying essential genes. *Nat. Biotechnol.* **34**, 631–633 (2016).
46. M. F. Fraga, M. Esteller, Epigenetics and aging: The targets and the marks. *Trends Genet.* **23**, 413–418 (2007).
47. M. J. Jones, S. J. Goodman, M. S. Kobor, DNA methylation and healthy human aging. *Aging Cell* **14**, 924–932 (2015).
48. S. Pal, J. K. Tyler, Epigenetics and aging. *Sci. Adv.* **2**, e1600584 (2016).
49. W. Zhang, J. Qu, G. H. Liu, J. C. I. Belmonte, The ageing epigenome and its rejuvenation. *Nat. Rev. Mol. Cell Biol.* **21**, 137–150 (2020).
50. S. Peleg, C. Feller, A. G. Ladurner, A. Imhof, The metabolic impact on histone acetylation and transcription in ageing. *Trends Biochem. Sci.* **41**, 700–711 (2016).
51. H. Pan, D. Guan, X. Liu, J. Li, L. Wang, J. Wu, J. Zhou, W. Zhang, R. Ren, W. Zhang, Y. Li, J. Yang, Y. Hao, T. Yuan, G. Yuan, H. Wang, Z. Ju, Z. Mao, J. Li, J. Qu, F. Tang, G. H. Liu, SIRT6 safeguards human mesenchymal stem cells from oxidative stress by coactivating NRF2. *Cell Res.* **26**, 190–205 (2016).
52. Y. Kanfi, S. Naiman, G. Amir, V. Peshti, G. Zinman, L. Nahum, Z. Bar-Joseph, H. Y. Cohen, The sirtuin SIRT6 regulates lifespan in male mice. *Nature* **483**, 218–221 (2012).
53. N. Saksouk, N. Avvakumov, K. S. Champagne, T. Hung, Y. Doyon, C. Cayrou, E. Paquet, M. Ullah, A. J. Landry, V. Cote, X. J. Yang, O. Gozani, T. G. Kutateladze, J. Cote, HBO1 HAT complexes target chromatin throughout gene coding regions via multiple PHD finger interactions with histone H3 tail. *Mol. Cell* **33**, 257–265 (2009).
54. B. Bernardes de Jesus, E. Vera, K. Schneeberger, A. M. Tejera, E. Ayuso, F. Bosch, M. A. Blasco, Telomerase gene therapy in adult and old mice delays aging and increases longevity without increasing cancer. *EMBO Mol. Med.* **4**, 691–704 (2012).
55. M. Jaskelioff, F. L. Muller, J. H. Paik, E. Thomas, S. Jiang, A. C. Adams, E. Sahin, M. Kost-Alimova, A. Protopopov, J. Cadinanos, J. W. Horner, E. Maratos-Flier, R. A. Depinho, Telomerase reactivation reverses tissue degeneration in aged telomerase-deficient mice. *Nature* **469**, 102–106 (2011).
56. A. Tomas-Loba, I. Flores, P. J. Fernandez-Marcos, M. L. Cayuela, A. Maraver, A. Tejera, C. Borras, A. Matheu, P. Klatt, J. M. Flores, J. Vina, M. Serrano, M. A. Blasco, Telomerase reverse transcriptase delays aging in cancer-resistant mice. *Cell* **135**, 609–622 (2008).
57. N. Davidsohn, M. Pezone, A. Vernet, A. Graveline, D. Oliver, S. Slomovic, S. Punthambaker, X. Sun, R. Liao, J. V. Bonventre, G. M. Church, A single combination gene therapy treats multiple age-related diseases. *Proc. Natl. Acad. Sci. U.S.A.* **116**, 23505–23511 (2019).
58. J. Yang, J. Li, K. Suzuki, X. Liu, J. Wu, W. Zhang, R. Ren, W. Zhang, P. Chan, J. C. Izpisua Belmonte, J. Qu, F. Tang, G. H. Liu, Genetic enhancement in cultured human adult stem cells conferred by a single nucleotide recoding. *Cell Res.* **27**, 1178–1181 (2017).
59. H. Kim, H. Jeong, Y. Cho, J. Lee, K. T. Nam, H. W. Lee, Disruption of the Tff1 gene in mice using CRISPR/Cas9 promotes body weight reduction and gastric tumorigenesis. *Lab Anim Res* **34**, 257–263 (2018).
60. T. Wang, J. J. Wei, D. M. Sabatini, E. S. Lander, Genetic screens in human cells using the CRISPR-Cas9 system. *Science* **343**, 80–84 (2014).
61. S. Anders, W. Huber, Differential expression analysis for sequence count data. *Genome Biol.* **11**, R106 (2010).
62. M. Altaf-Ul-Amin, Y. Shinbo, K. Mihara, K. Kurokawa, S. Kanaya, Development and implementation of an algorithm for detection of protein complexes in large interaction networks. *BMC Bioinformatics* **7**, 207 (2006).
63. D. A. Orlando, M. W. Chen, V. E. Brown, S. Solanki, Y. J. Choi, E. R. Olson, C. C. Fritz, J. E. Bradner, M. G. Guenther, Quantitative ChIP-seq normalization reveals global modulation of the epigenome. *Cell Rep.* **9**, 1163–1170 (2014).

Acknowledgments: We acknowledge Y. Yu (IBP, CAS) for providing the *Drosophila* S2 cell line; W. Wei (PKU) for advice on CRISPR-Cas9–based screens; Y. Diao (UCSD) for advice on Hi-C analysis; L.Bai, R. Bai, J. Lu, Q. Chu, Y. Yang, X. Zhuo, and S. Ma for administrative assistance; X. Liu for assisting with bioinformatics analyses: J. Jia and J. Jiao for assisting with animal experiments; J. Jia for the FACS; J. Hao for pathological analysis; and X. Shi, L. Zhou, and X. Wu for management of laboratory animals. We thank all the members of the Liu laboratory for discussion and technical assistance. High-throughput sequencing data were processed on the "Era" petascale supercomputer of Computer Network Information Center of Chinese Academy of Sciences. **Funding:** This work was supported by the National Key Research and Development Program of China (2018YFC2000100) (to J.Q.), the Strategic Priority Research Program of the Chinese Academy of Sciences (XDA16010100) (to G.-H.L., J.Q., W.Z., and M.S.), the National Key Research and Development Program of China [2017YFA0103304 and 2017YFA0102802 (to W.Z.), 2018YFA0107203 (to J.Q.), 2015CB964800 (to G.-H.L.), 2018YFC2000400 (to J.L.), and 2017YFA0102702 (to F.T.), 2020YFA0804000 and 2020YFA0112201 (to G.-H.L.), 2020YFA0113400 (to M.S.)], the National Natural Science Foundation of China [81625009, 81921006, 91749202, and 81861168034 (to G.-H.L.); 81671377, 81822018, and 91749123 (to W.Z.); 31671429 and 91949209 (to J.Q.); 81701388 and 82071588 (to S.W.); 81870228 and 81922027 (to M.S.); 81801399 (to J.L.); 31801010 (to W.L.); 31900523 (to S.S.); and 32000510 (to Y.F.)], Program of Beijing Municipal Science and Technology Commission (Z191100001519005) (to G.-H.L.), Beijing Natural Science Foundation (Z190019) (to G.-H.L.), K.C. Wong Education Foundation [GJTD-2019-06 (to J.Q.) and GJTD-2019-08 (to W.Z.)], the Key Research Program of the Chinese Academy of Sciences (KFZD-SW-221) (to J.Q.), Advanced Innovation Center for Human Brain Protection (3500-1192012) (to G.-H.L.), Beijing Municipal Commission of Health and Family Planning (PXM2018_026283_000002) (to G.-H.L.), Youth Innovation Promotion Association of CAS (2016093) (to W.Z.), grants from Young Elite Scientists Sponsorship Program by CAST (2017QNRC001) (to J.L.), grants from International Partnership Program of Chinese Academy of Sciences (152111KYSB20160004) (to Q.Z.),152111KYSB20160004 (to Y.L.), State Key Laboratory of Membrane Biology, State Key Laboratory of Stem Cell and Reproductive Biology, and Beijing Advanced Innovation Center for Genomics (ICG) at Peking University. **Author contributions:** G.-H.L., F.T., J.Q., and W.Z. conceptualized the work and supervised overall experiments. W.W. performed the phenotypic and mechanistic analyses. Y.Z. and Q.J. performed bioinformatics analyses with assistance from Z.L. S.S. performed experiments in human hepatocytes. W.L. performed animal experiments. J.L. performed the RNA-seq library construction in *KAT7*-depleted WS hMPCs, and Z.W. performed the plasmid construction. Y.F. and F.L. performed immunostaining and tissue section analyses. G.-H.L., F.T., J.Q., W.Z., W.W., S.S., and M.S. performed data analysis. G.-H.L., F.T., J.Q., W.Z., W.W., S.S., M.S., S.W., Q.Z., J.C.I.B., and C.R.E. wrote and reviewed the manuscript. **Competing interests:** The authors declare that they have no competing interests. **Data and materials availability:** All data associated with this study are present in the paper or the Supplementary Materials. The raw sequencing data and processed data used in this study have been deposited in the Gene Expression Omnibus (GEO) database under the accession number GSE124197.

Submitted 10 June 2020
Accepted 4 December 2020
Published 6 January 2021
10.1126/scitranslmed.abd2655

Citation: W. Wang, Y. Zheng, S. Sun, W. Li, M. Song, Q. Ji, Z. Wu, Z. Liu, Y. Fan, F. Liu, J. Li, C. R. Esteban, S. Wang, Q. Zhou, J. C. I. Belmonte, W. Zhang, J. Qu, F. Tang, G.-H. Liu, A genome-wide CRISPR-based screen identifies *KAT7* as a driver of cellular senescence. *Sci. Transl. Med.* **13**, eabd2655 (2021).

Science Translational Medicine

A genome-wide CRISPR-based screen identifies *KAT7* as a driver of cellular senescence

Wei Wang, Yuxuan Zheng, Shuhui Sun, Wei Li, Moshi Song, Qianzhao Ji, Zeming Wu, Zunpeng Liu, Yanling Fan, Feifei Liu, Jingyi Li, Concepcion Rodriguez Esteban, Si Wang, Qi Zhou, Juan Carlos Izpisua Belmonte, Weiqi Zhang, Jing Qu, Fuchou Tang and Guang-Hui Liu

Sci Transl Med **13**, eabd2655.
DOI: 10.1126/scitranslmed.abd2655

Slowing cellular senescence

Whereas cellular senescence is known to promote aging, many of the mechanisms controlling this process remain poorly understood. Using human mesenchymal precursor cells (hMPCs) carrying pathogenic mutations of t he premature aging diseases Werner syndrome and Hutchinson-Gilford progeria syndrome, the authors conducted a genome-wide CRISPR-Cas9 –based screen to identify genes that could affect cellular senescence. They identified *KAT7*, a histone acetyltransferase gene, as a driver of senescence. Inactivation of Kat7 in mice aging normally and in prematurely aging progeroid mice extended their life span. Although KAT7 requires further study in other cell types, these experiments highlight the utility of genome-wide CRISPR-Cas9 screens and shed further light on mechanisms controlling senescence.